

# Large-scale real-time signal processing in physics experiments: The ALICE TPC FPGA pipeline

## ALICE TPC collaboration

J. Alme<sup>c</sup> T. Alt<sup>h,1</sup> C. Andreig V. Anguelov<sup>o</sup> H. Appelshäuser<sup>h</sup> M. Arslanbekov<sup>z</sup> R. Averbeck<sup>q</sup>  
 M. Ball<sup>f</sup> G. G. Barnaföldi<sup>y</sup> P. Becht<sup>o,q</sup> R. Bellwied<sup>v</sup> A. Berdnikova<sup>o</sup> B. Blidaru<sup>o,q</sup>  
 L. Boldizsár<sup>y</sup> L. Bratrud<sup>h</sup> P. Braun-Munzinger<sup>q</sup> M. Bregant<sup>t</sup> C. L. Britton<sup>m</sup> H. Büsching<sup>h</sup>  
 H. Caines<sup>z</sup> P. Chatzidakis<sup>o,2</sup> P. Christiansen<sup>j</sup> T. M. Cormier<sup>†m</sup> L. Döpper<sup>f</sup> R. Ehlers<sup>z,3</sup>  
 L. Fabbietti<sup>p</sup> F. Flor<sup>v</sup> J. J. Gaardhøje<sup>l</sup> M. G. Munhoz<sup>t</sup> C. Garabatos<sup>q</sup> P. Gasik<sup>q</sup> Á. Gera<sup>y</sup>  
 P. Glässel<sup>o</sup> N. Grünwald<sup>o</sup> T. Gündem<sup>h</sup> T. Gunji<sup>x</sup> H. Hamagaki<sup>k</sup> J. W. Harris<sup>z</sup> P. Hauer<sup>f</sup>  
 E. Hellbär<sup>h,2</sup> H. Helstrup<sup>e</sup> A. Herghelegiu<sup>g</sup> H. D. Hernandez Herrera<sup>t,4</sup> Y. Hou<sup>q,5</sup>  
 C. Hughes<sup>w,6</sup> M. Ivanov<sup>q</sup> J. Jäger<sup>h</sup> Y. Ji<sup>q</sup> J. Jung<sup>h</sup> M. Jung<sup>h</sup> B. Ketzer<sup>f</sup> S. Kirsch<sup>h,1</sup>  
 M. Kleiner<sup>h</sup> A. G. Knospe<sup>v</sup> M. Korwieser<sup>p</sup> M. Kowalski<sup>r</sup> L. Lautner<sup>p</sup> M. Lesch<sup>p</sup>  
 C. Lippmann<sup>q,1</sup> G. Mantzaridis<sup>p</sup> R. D. Majka<sup>†z</sup> A. Marin<sup>q</sup> C. Markert<sup>s</sup> S. Masciocchi<sup>q</sup>  
 A. Matyja<sup>r</sup> M. Meres<sup>a</sup> D. L. Mihaylov<sup>p</sup> D. Miśkowiec<sup>q</sup> R. H. Munzer<sup>h</sup> H. Murakami<sup>x</sup>  
 K. Münning<sup>f</sup> A. Nassirpour<sup>j,7</sup> C. Nattrass<sup>w</sup> B. S. Nielsen<sup>l</sup> W. A. V. Noije<sup>t</sup> A. C. Oliveira Da  
 Silva<sup>w</sup> A. Oskarsson<sup>j</sup> K. Oyama<sup>k</sup> L. Österman<sup>j</sup> Y. Pachmayer<sup>o</sup> G. Paić<sup>i</sup> M. Petris<sup>g</sup>  
 M. Petrovici<sup>g</sup> M. Planinic<sup>n</sup> J. Rasson<sup>m</sup> K. F. Read<sup>m</sup> A. Rehman<sup>c</sup> R. Renfordt<sup>h</sup> A. Riedel<sup>p</sup>  
 K. Røed<sup>b</sup> D. Röhrl<sup>c</sup> E. Rubio<sup>o</sup> A. Rusu<sup>m</sup> S. Sadhu<sup>f</sup> B. C. S. Sanches<sup>t</sup> J. Schambach<sup>s</sup>  
 A. Schmah<sup>q</sup> C. Schmidt<sup>q</sup> A. Schmier<sup>w</sup> K. Schweda<sup>q</sup> D. Sekihata<sup>x</sup> D. Silvermyr<sup>j</sup> B. Sitar<sup>a</sup>  
 N. Smirnov<sup>z</sup> H. K. Soltveit<sup>o</sup> C. Sonnabend<sup>d,q</sup> S. P. Sorensen<sup>w</sup> J. Stachel<sup>o</sup> L. Šerkšnytė<sup>p,2</sup>  
 G. Tambave<sup>c,8</sup> K. Ullaland<sup>c</sup> B. Ulukutlu<sup>p</sup> D. Varga<sup>y</sup> O. Vazquez Rueda<sup>j,9</sup> B. Voss<sup>q</sup>  
 J. Wiechula<sup>h</sup> B. Windelband<sup>o</sup> J. Wilkinson<sup>q</sup> J. Witte<sup>o,q</sup> A. Yadav<sup>f</sup> F. Zanone<sup>o</sup> S. Zhu<sup>q,10</sup>

<sup>a</sup>Comenius University Bratislava, Faculty of Mathematics, Physics and Informatics, Bratislava, Slovakia

<sup>b</sup>Department of Physics, University of Oslo, Norway

<sup>c</sup>Department of Physics and Technology, University of Bergen, Norway

<sup>d</sup>European Organization for Nuclear Research (CERN), Geneva, Switzerland

<sup>1</sup>Corresponding author.

<sup>2</sup>Now at European Organization for Nuclear Research (CERN), Geneva, Switzerland

<sup>†</sup>Deceased.

<sup>3</sup>Now at Lawrence Berkeley National Laboratory, Berkeley, California, USA

<sup>4</sup>Now at SLAC National Accelerator Laboratory, Menlo Park, California, USA

<sup>5</sup>Also at China University of Geosciences, Wuhan, China

<sup>6</sup>Now at Iowa State University, Ames, Iowa, USA

<sup>7</sup>Now at Sejong University, Seoul, South Korea

<sup>8</sup>Now at National Institute of Science Education and Research (NISER), Bhubaneswar, India

<sup>9</sup>Now at University of Houston, Texas, USA

<sup>10</sup>Also at University of Science and Technology of China (USTC), Hefei, China

<sup>e</sup>*Faculty of Engineering and Science, Western Norway University of Applied Sciences, Bergen, Norway*

<sup>f</sup>*Helmholtz-Institut für Strahlen- und Kernphysik, Rheinische Friedrich-Wilhelms-Universität Bonn, Germany*

<sup>g</sup>*Horia Hulubei National Institute of Physics and Nuclear Engineering, Bucharest, Romania*

<sup>h</sup>*Institut für Kernphysik, Johann Wolfgang Goethe-Universität Frankfurt, Germany*

<sup>i</sup>*Instituto de Ciencias Nucleares, Universidad Nacional Autónoma de México, Mexico City, Mexico*

<sup>j</sup>*Lund University Department of Physics, Division of Particle Physics, Lund, Sweden*

<sup>k</sup>*Nagasaki Institute of Applied Science, Nagasaki, Japan*

<sup>l</sup>*Niels Bohr Institute, University of Copenhagen, Denmark*

<sup>m</sup>*Oak Ridge National Laboratory, Oak Ridge, Tennessee, USA*

<sup>n</sup>*Physics department, Faculty of science, University of Zagreb, Croatia*

<sup>o</sup>*Physikalisches Institut, Ruprecht-Karls-Universität Heidelberg, Germany*

<sup>p</sup>*Physik Department, Technische Universität München, Munich, Germany*

<sup>q</sup>*Research Division and ExtreMe Matter Institute EMMI, GSI Helmholtzzentrum für Schwerionenforschung GmbH, Darmstadt, Germany*

<sup>r</sup>*The Henryk Niewodniczanski Institute of Nuclear Physics, Polish Academy of Sciences, Cracow, Poland*

<sup>s</sup>*The University of Texas at Austin, Texas, USA*

<sup>t</sup>*Universidade de S*

<sup>,ao Paulo (USP), Brazil</sup>

<sup>v</sup>*University of Houston, Texas, USA*

<sup>w</sup>*University of Tennessee, Knoxville, Tennessee, USA*

<sup>x</sup>*University of Tokyo, Japan*

<sup>y</sup>*Wigner Research Centre for Physics, Budapest, Hungary*

<sup>z</sup>*Yale University, New Haven, Connecticut, USA*

*E-mail: [Torsten.Alt@cern.ch](mailto:Torsten.Alt@cern.ch), [C.Lippmann@gsi.de](mailto:C.Lippmann@gsi.de)*

**ABSTRACT:** For LHC Run 3, the ALICE Time Projection Chamber (TPC) was upgraded to operate in continuous readout mode. Interaction rates of up to 50 kHz in Pb–Pb collisions require real-time processing of more than 3 TB s<sup>-1</sup> of raw detector data. This requirement is met by a custom FPGA-based processing pipeline that performs the complete front-end data treatment fully in-stream, including common-mode correction, pedestal subtraction, ion-tail filtering, zero suppression, and dense data packing.

A central element of the design is a highly parallel common-mode correction algorithm operating directly on the streaming data. It robustly identifies signal-free readout channels on a time-bin basis and applies pad-dependent scaling to compensate for local variations in capacitive coupling in the gas electron multiplier (GEM) readout. In combination with pedestal subtraction and ion-tail filtering, this enables accurate baseline restoration under extreme high-occupancy conditions, preventing signal loss while efficiently suppressing noise prior to zero suppression.

The pipeline operates continuously at the full detector bandwidth and reduces the raw input rate of approximately 3 TB s<sup>-1</sup> to about 900 GB s<sup>-1</sup> for Pb–Pb collisions at the target interaction rate. Overall, it represents a large-scale FPGA-based real-time signal-processing implementation for high-energy physics detector readout.

**KEYWORDS:** Gaseous detectors, Micropattern gaseous detectors (GEM), Time Projection Chambers (TPC), Detector readout systems, Online data processing in FPGAs

---

## Contents

<b>1 The upgraded ALICE TPC</b>	<b>2</b>
1.1 Overview on the data processing chain	2
1.2 Front-end electronics	3
1.2.1 SAMPA	3
1.2.2 Giga-Bit Transceiver	4
1.3 Common readout unit	5
1.4 Timing	6
1.5 Synchronization of ADC sampling clocks and data streams	7
1.6 Data format of the GBT frames	8
1.7 Readout modes	8
<b>2 User logic for data processing</b>	<b>8</b>
2.1 Data format of the processing pipeline	9
2.2 Overview of the UL processing pipeline	11
2.3 Slow Control Network (SCN)	12
2.4 Resource utilisation	13
2.5 Input stage	13
2.5.1 GBT frame decoder	13
2.5.2 Global aligner	14
2.5.3 Resync controller	16
2.5.4 Pattern generator	16
2.6 Processing stage	17
2.6.1 Common-mode correction	17
2.6.2 Pedestal subtraction and zero suppression	27
2.6.3 Ion-tail filter	29
2.6.4 Integrated digital currents	31
2.7 Output stage	33
2.7.1 Data format	33
2.7.2 Merging and packing pipeline	34
<b>3 User Logic for auxiliary systems</b>	<b>36</b>
3.1 Laser control	37
3.2 Calibration pulser control	37
3.3 Readout of the high voltage current monitor system	37
<b>4 Summary and discussion</b>	<b>39</b>

---

## 1 The upgraded ALICE TPC

The Time Projection Chamber (TPC) of A Large Ion Collider Experiment (ALICE), located at the CERN Large Hadron Collider (LHC), served as the main tracking detector during Runs 1 and 2 (2009–2018), employing multi-wire proportional chambers (MWPCs) with cathode-pad signal readout [1].

To meet the demands of LHC Runs 3 and 4, the TPC underwent a major upgrade during the LHC long shutdown from 2019 to 2021. The upgrade involved replacing the MWPCs with new readout chambers based on GEM technology and installing entirely new front-end electronics in order to continuously read the signals on the anode pads [2]. This modernization was driven by the need to accommodate much higher interaction rates, reaching up to 50 kHz in lead–lead (Pb–Pb) collisions.

The ALICE TPC is a large cylindrical detector, divided longitudinally into two halves by a central drift electrode. Each end plate, located at the ends of the cylinder, houses the readout chambers and is subdivided into 18 azimuthal sectors. Every sector contains Inner ReadOut Chambers (IROCs) and Outer ReadOut Chambers (OROCs). The new GEM-based readout chambers use a stack of four GEM foils for gas amplification. Unlike the previous design, the upgraded system does not use an ion gating grid. As a result, ion backflow—i.e., the return of positive ions into the drift volume—must be minimized. This is achieved through a specially optimized amplification structure and a thoroughly tuned high-voltage configuration across the GEM stack (cf. [2]).

The upgraded TPC has been successfully commissioned and is now fully operational, effectively supporting the physics objectives of ALICE in high-luminosity heavy-ion collisions [3, 4]. In this publication, we describe in detail the readout system of the ALICE TPC, with a particular focus on the data processing algorithms implemented in firmware on the readout cards that receive data from the TPC front-end electronics.

### 1.1 Overview on the data processing chain

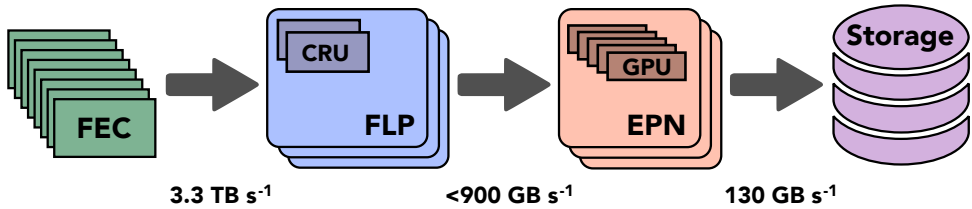


**Figure 1.** TPC data processing chain. The front-end electronics continuously transmit all sampled data off-detector. In the First-Level Processors (FLP), each hosting two or three FPGA-based readout cards, known as Common Readout Units (CRUs), the data are corrected for specific detector effects and reduced in size. The resulting reduced data stream is distributed to the Event-Processing Nodes (EPNs). Each EPN performs online calibration, reconstruction, data reduction and data compression, before the data are directed to permanent storage.

The full data processing chain is illustrated schematically in Fig. 1. At the front-end electronics (cf. Section 1.2), signals from the 524 160 anode readout pads are amplified, shaped, and continuously sampled and digitized at a rate of 5 MHz. The digitized data are multiplexed into

6552 radiation-tolerant optical readout links. At this stage, no data reduction is applied, ensuring that all raw detector information is available for subsequent correction of detector-specific effects at the next stage. The total data rate from the [TPC](#) amounts to  $3.3 \text{ TB s}^{-1}$ . The data are received by a total of 360 Common Readout Units (CRUs) (cf. Section 1.3), each containing a large field-programmable gate array (FPGA), which is programmed to perform data processing and reduction tasks (cf. Section 2).

The performance of the [GEM](#)-based signal amplification is affected by two effects: (i) baseline fluctuations induced by the *common-mode effect*, and (ii) characteristic distortions in the pulse shape caused by slowly drifting ions in the induction gap (*ion tails*). Both phenomena are described in detail in [5] and are corrected in the [CRU FPGA](#). Zero-suppression is applied only after these corrections, so that the data volume is effectively reduced without loss of information.

The [CRUs](#) are installed in 144 First-Level Processors (FLPs), which are dedicated readout computers, each hosting two or three [CRUs](#), depending on data throughput. Data are pushed from the [FLPs](#) to the Event-Processing Nodes (EPNs) farm via custom distribution software deployed on both farms. For Pb–Pb collisions at 50 kHz, the total data rate remains below  $900 \text{ GB s}^{-1}$ .

The continuous stream is segmented into Time Frames (TFs) of configurable length (currently 2.85 ms).<sup>1</sup> Each [FLP](#) produces Sub-Time Frames (STFs) from a TPC subset. While not all [EPNs](#) receive all [STFs](#), each one receives the complete set required to assemble a full [TF](#).

Since [TPC](#) calibration and compression require track information, [EPNs](#) perform full online track reconstruction during data taking. Each server is equipped with eight [GPUs](#), which handle tracking and calibration entirely.

The output stream to storage is about  $130 \text{ GB s}^{-1}$  for Pb–Pb at 50 kHz. Further asynchronous processing, on the [EPNs](#) or on the [ALICE](#) computing grid, refines the data to final precision.

## 1.2 Front-end electronics

The front-end card (FEC) for the [ALICE TPC](#) is described in detail in [2] and illustrated schematically in Fig. 2. It comprises the front-end application-specific integrated circuit (ASIC) SAMPA, the Giga-Bit Transceiver (GBT) chipset and Versatile Link components, along with auxiliary circuitry such as voltage regulators and temperature sensors.

### 1.2.1 SAMPA

The SAMPA [6] [ASIC](#) was specifically designed for the upgraded front-end electronics of both the [TPC](#) and the [ALICE](#) Muon Chambers [7]. The [GBT](#) and Versatile Link components were developed at CERN to provide a radiation-tolerant, bidirectional optical link for data transmission as well as timing and control between the detector and off-detector systems.

The SAMPA is implemented in 130 nm CMOS technology with a nominal supply voltage of 1.25 V. It features 32 channels with configurable input polarity and offers three combinations of shaping time and gain. Each channel includes a charge-sensitive amplifier, a semi-Gaussian shaper, and a 10-bit analog-to-digital converter (ADC). A digital signal processor (DSP) is integrated to provide digital filtering and data compression. Data output is handled via 11 serial electrical links (E-links), each operating at a configurable frequency.

---

<sup>1</sup>The time frames are sized to fit in the graphics processing unit (GPU) memory for efficient processing on the [EPNs](#).

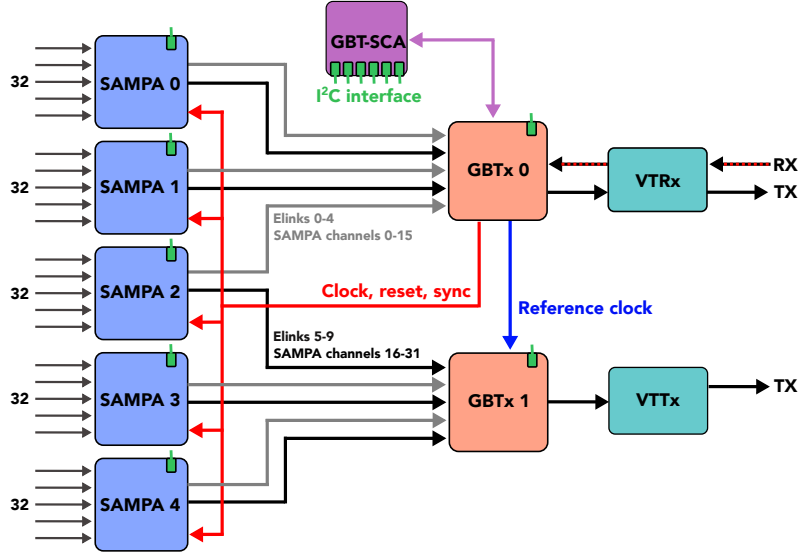


**Figure 2.** Schematic of the **TPC** Front-End Card (FEC). Five 32-channel SAMPA chips process pad signals and send them to two **GBTx** chips for multiplexing and off-detector transfer. The SAMPA chips are operated in split mode, where the data from two groups of channels can be sent to different destinations. The **FEC** connects via three optical fibers, two Tx for data and one Rx for commands, configuration, and clock. The clock is distributed from **GBTx0**. All configuration is handled by the **GBT-SCA** over  $I^2C$ .

Each **FEC** hosts five SAMPA chips, providing a total of 160 readout channels. In operation, the SAMPA is configured in direct ADC sampling (DAS) mode, wherein the **DSP** is bypassed and powered down. In this mode, all **ADC** data are streamed continuously, and the output contains no data markers. Each SAMPA generates a data rate of  $1.6 \text{ Gbit s}^{-1}$ , transmitted via ten **E-links** at  $160 \text{ Mbit s}^{-1}$  each.<sup>2</sup> The 11th **E-link** carries the 5 MHz **ADC** sampling clock, allowing verification of alignment and phase consistency across the full **TPC**. This results in a total per-chip data rate of  $1.76 \text{ Gbit/s}^3$ .

The SAMPA operates in split mode, whereby the 32 readout channels are divided into two groups (0–15 and 16–31), each of which may be sent to a dedicated upstream receiver. **E-links** 0–4 carry data from the first group, and **E-links** 5–9 from the second. Each 16-channel group is serialized over 32 **E-link** clock cycles. In each pair of cycles, the lower and upper 5 bits of an **ADC** value are transmitted in parallel. For example, during the first cycle, the lower 5 bits of channel 0 and channel 16 are transmitted simultaneously; the next cycle transmits the upper 5 bits, and the process continues channel by channel.

### 1.2.2 Giga-Bit Transceiver

Two **GBTx** chips, **GBTx0** and **GBTx1**, multiplex the data and forward them to a versatile transceiver (**VTRx**) and a versatile twin transmitter (**VTTx**). The **VTRx** is a bidirectional optical transceiver, while the **VTTx** contains two transmit channels, one of which is used. Thus, each **FEC** employs

<sup>2</sup> $32 \text{ channels} \times 10 \text{ bit} \times 5 \text{ MHz} = 1.6 \text{ Gbit s}^{-1}$

<sup>3</sup> $11 \text{ E-links} \times 160 \text{ Mbit s}^{-1} = 1.76 \text{ Gbit s}^{-1}$

two optical Tx fibers for data transmission and one Rx fiber for receiving clock, configuration, and control signals.

Each **GBTx** receives data from two full SAMPAs. The fifth SAMPA routes the first channel group to **GBTx0** and the second to **GBTx1**. The 11th **E-link** from this chip is split to deliver the sampling clock to both **GBTx** devices.

The total input data rate per **GBTx** is  $4.48 \text{ Gbit s}^{-1}$ .<sup>4</sup> The Versatile Link operates at a line rate of  $4.8 \text{ Gbit s}^{-1}$  and delivers in wide-frame mode<sup>5</sup> as usable data bandwidth exactly the needed  $4.48 \text{ Gbit s}^{-1}$ . The total data rate per **FEC** is thus  $8.96 \text{ Gbit s}^{-1}$ , excluding monitoring overhead.

The Rx link from the **CRU** to the **FEC** has fixed and deterministic latency and is protected by forward error correction. It is used to transmit clock, control, and configuration data via the **VTRx** to **GBTx0**.

Finally, among the key components on the **FEC** is the **GBT-SCA** chip, responsible for configuration and monitoring. It communicates with other components on the board using the  $\text{I}^2\text{C}$  protocol.

### 1.3 Common readout unit

The common readout unit (CRU) is a custom **FPGA** card [8] developed collaboratively by LHCb [9] and **ALICE** [10]. It follows a PCI express (PCIe) form factor (three-quarter length, standard height, dual-slot) and complies with **PCIe** specifications. The board is based on an Intel<sup>TM</sup> Arria 10 **FPGA** featuring 72 serializer/deserializers (SerDess), of which 16 are dedicated to the host interface with the PC. The **CRU** also provides an interface to the timing, trigger and control - passive optical network (TTC-PON) for receiving trigger and timing information distributed by the experiment. The front-end electronics (FEE) are connected via up to 48 bi-directional optical links, each supporting bandwidths of up to  $10 \text{ Gbit s}^{-1}$  in both directions.

The **CRU** firmware consists of a Common Logic<sup>6</sup> including common design components shared across several **ALICE** subdetectors and a subdetector-specific User Logic (UL). For the **TPC**, two distinct top-level design **UL** units have been implemented, each serving fundamentally different purposes:

- 360 **CRUs** operate with the data-processing **UL** to handle collision data and transmit it to the **FLPs** (cf. Section 2), and
- an additional **CRU** performs synchronized control of the **TPC** laser and pulser systems, and reads out the monitoring system of the **GEM** currents (cf. Section 3).

Since the latter functionality requires only modest logic resources, both design units are integrated into a single TPC user logic (TPC UL), simplifying firmware build and deployment. The

---

<sup>4</sup> $(5 \times 5 + 3) \text{ E-links} \times 160 \text{ Mbit s}^{-1} = 4.48 \text{ Gbit s}^{-1}$

<sup>5</sup>The standard **GBT** frame format includes forward error correction, which reduces the effective data rate to  $3.2 \text{ Gbit s}^{-1}$ . To achieve higher throughput, the wide-frame mode disables forward error correction, thereby increasing the usable data rate at the expense of error protection. In the case of **ALICE**, this trade-off is acceptable: the radiation background is significantly lower than in typical Versatile Link applications, so the absence of forward error correction does not pose a concern for data integrity.

<sup>6</sup>Maintained by a central development team.

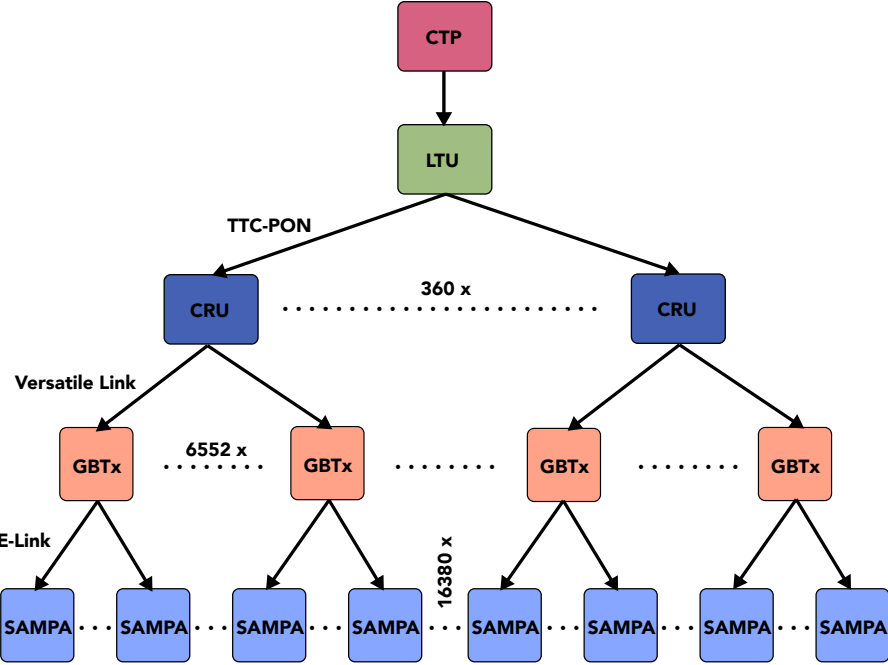


**Figure 3.** Clock and trigger distribution tree for the [ALICE TPC](#).

S

operational mode—i.e., which of the two design units is active—can be selected as needed. In the remainder of this paper, these two configurations are treated as distinct [UL](#) flavors.

#### 1.4 Timing

At the [LHC](#), the fundamental units of time are defined by the orbit number and the bunch crossing number. An orbit corresponds to the time it takes for a particle bunch to complete a full revolution around the accelerator ring: approximately 89.1  $\mu$ s. A bunch crossing refers to the event in which two particle bunches, traveling in opposite directions, pass through an interaction point.<sup>7</sup> The bunch crossing rate, approximately 40 MHz, defines the fundamental clock frequency distributed from the [LHC](#) to the experiments. All accelerator operations, data acquisition systems, and detector electronics are synchronized based on these time units.

In [ALICE](#), the distribution of the bunch crossing clock, along with crucial timing information such as orbit and bunch crossing counters<sup>8</sup> and trigger signals, is managed by the Timing, Trigger and Control (TTC) system. Figure 3 illustrates the clock and trigger distribution network for the [TPC](#), which forms part of the global [ALICE TTC](#) infrastructure.

The Central Trigger Processor (CTP) serves as the central synchronization node for [ALICE](#), interfacing with the [LHC](#) to generate the clock, timing, and trigger signals used across the experi-

<sup>7</sup>In actual beam operation, not all bunches are filled with particles, and therefore not every bunch crossing results in a collision.

<sup>8</sup>After each completed orbit, corresponding to 3564 bunch crossings, the bunch-crossing counter resets to 0, and the orbit counter increments by one.

ment. This information is passed to the detector-specific Local Trigger Unit (LTU), which encodes it into a high-speed serial signal. The signal is then distributed to all **CRUs** via the **TTC-PON**.

Each **CRU** recovers the distributed clock and extracts the trigger message. The recovered clock is phase-synchronous across all **CRUs** and is used to drive communication between the **CRUs** and the **GBTx0** chips on the **FECs**. Each **GBTx0** generates the 160 MHz **E-link** clock, which is then distributed to the SAMPA chips. The SAMPA chips internally derive the 5 MHz **ADC** sampling clock from the **E-link** clock using a clock divider.<sup>9</sup>

A key characteristic of the Versatile Link and the **GBTx** is their guaranteed fixed and deterministic latency on the Rx path to the **FEC**. This ensures that signals transmitted over the Versatile Link arrive with identical timing on the **E-link** pins of all **GBTx** devices across the **FECs**, thereby enabling system-wide synchronization.

The trigger message sent from the **LTU** and received by the **CRU** at the 40 MHz bunch crossing rate includes orbit and bunch-crossing numbers along with trigger bits. This information is not forwarded to the **FECs**. Instead, the timing-critical operation of the SAMPAAs is controlled directly by the **CRU** via the fixed-latency path described above, using dedicated signal lines between the corresponding SAMPA and **GBTx** pins (cf. Section 1.5).

The data collected from the input links are segmented into time slices called heartbeat frames (HBFs). An **HBF** corresponds to the data bounded by two heartbeat signals (HB), which are periodic signals synchronized to the LHC orbit at a frequency of 11.223 kHz. An **HBF** represents the smallest unit of data processed at the **FLP** level. Each **HBF** is tagged with an HB ID, which includes the orbit number, bunch crossing number, and trigger information.

At the **FLP**, a configurable number of consecutive **HBFs** (currently 32) are merged to form an **STF**. At the **EPNs**, all **STFs** from the various **FLPs** that correspond to the same time period are aggregated into a **TF** (cf. Section 1.1).

## 1.5 Synchronization of ADC sampling clocks and data streams

The SAMPA chips generate the **ADC** clock internally from the phase-synchronous 160 MHz **E-link** clock using a simple clock divider within each SAMPA chip. Since this divider begins counting immediately upon power-up, the resulting **ADC** clock phase can differ between SAMPAAs, even between those on the same FEC.

To synchronize the **ADC** clocks across all SAMPA chips on the **TPC**, each SAMPA provides a physical *RESET* pin, which is directly connected to an **E-link** on the **GBTx0**. This **E-link** is controlled by the **CRU**, and due to the fixed-latency characteristics of the **GBT** system, the timing of the *RESET* signal is deterministic. This allows the **CRU** to synchronously reset all SAMPAAs connected to it.

For global synchronization of the entire **TPC**, a reference signal from the **TTC** system can be employed. Suitable **TTC** references include a dedicated **TPC RESET** trigger, a specific bunch-crossing identifier, or every *N*th **LHC** orbit. Any such reference can be mapped inside the **CRU** to generate a synchronized *RESET*, which is then distributed to all connected SAMPA chips. A dedicated module in the Common Logic, the Pattern Player, performs this mapping by converting

---

<sup>9</sup>This approach avoids the need for a phase-locked loop (PLL), which is less reliable in radiation-prone environments.

the selected **TTC** reference into predefined pattern sequences that are subsequently transmitted to the SAMPAAs.

As detailed in Section 1.2, the SAMPA chips operate in **DAS** mode, in which the stream of **ADC** samples contains no embedded metadata or framing markers. Instead, the mapping between each **ADC** value and its corresponding channel is inferred solely from its position in the continuous output stream. To ensure correct alignment, a dedicated **SYNC** pattern is transmitted at the beginning of each stream, marking its start. After sending this pattern, the SAMPA enters a deterministic mode in which it cyclically transmits the **ADC** values from all input channels in a fixed order. One full cycle of these channel-ordered **ADC** values is referred to as a *time-bin*.

Upon issuing a **RESET**, the SAMPA automatically sends the **SYNC** pattern at the beginning of the next data transmission. Additionally, the **SYNC** pattern can be triggered manually via a dedicated **ENABLE** pin on the SAMPA, which, like the **RESET** pin, is connected to an **E-link** and thus controllable via the **CRU**.

For details on re-synchronization during decoding of the received data in the **TPC UL**, refer to Section 2.5.3.

## 1.6 Data format of the GBT frames

Each **FEC** uses two **GBTx** chips to collect, arrange, and transmit the data from its five connected SAMPA chips. The outgoing data are packaged into **GBT** frames, each consisting of 120 bits. In wide-frame mode (cf. Section 1.2.2), 112 of these bits are available for user data. Since **GBT** frames are transmitted at the LHC clock frequency of 40 MHz, the effective user-data bandwidth amounts to  $4.48 \text{ Gbit s}^{-1}$ .<sup>10</sup> The **GBTx** chips acquire data from 28 connected **E-link** inputs operating at 160 MHz. Each **GBT** frame thus encapsulates four consecutive bits per **E-link**.<sup>11</sup>

To encode the 32 **ADC** samples generated in a single **ADC** clock cycle (one time-bin), eight **GBT** frames are required.<sup>12</sup> Within the **CRU** firmware, these **GBT** frames are demultiplexed and unpacked on a per-link basis (cf. Section 2.5.1).

## 1.7 Readout modes

Although the data stream from **FEE** to the **CRUs** is inherently continuous, the **CRU** supports two distinct modes for forwarding data to the **FLPs**. In *continuous readout mode*, all data are transmitted to the **FLP**, with triggers embedded as metadata for reference during downstream processing. In *triggered readout mode*, data are transmitted to the **FLP** only for predefined time windows, and only in response to valid triggers.

## 2 User logic for data processing

The **TPC** user logic (UL) constitutes the subdetector-specific portion of the **CRU FPGA** firmware, responsible for processing raw **TPC** data. Within the **UL**, the fundamental data unit is defined as an **ADC** measurement acquired at a given time-bin from a single SAMPA channel. These measurements are hereafter referred to as *samples*.

---

<sup>10</sup> $112 \text{ bits} \times 40 \text{ MHz} = 4.48 \text{ Gbit s}^{-1}$

<sup>11</sup> $(5 \times 5 + 3) \text{ E-links} \times 4 \text{ bits} = 112 \text{ bits}$

<sup>12</sup> $8 \times 112 \text{ bits} \times 5 \text{ MHz} (\text{ADC sampling clock}) = 4.48 \text{ Gbit s}^{-1}$

During processing, the samples are sequentially propagated through multiple firmware stages, where correction operations are applied. To support these operations with increased numerical precision, the 10-bit resolution of the SAMPA chip [ADC](#) is extended to 12 bits.

The [UL](#) architecture is constrained by the data throughput requirements and available [FPGA](#) resources. It must sustain the processing of up to 1600 channels, each generating a new sample every 200 ns (5 MHz [ADC](#) sampling rate). In addition, it must implement multiple correction algorithms optimized for [TPC](#) operational conditions. These algorithms are classified according to processing scope:

1. Per-channel, multi-time-bin operations – Each channel is processed independently across time bins, often requiring feedback to maintain state between iterations. This category includes digital filtering operations, e.g., the ion-tail filter (cf. Section [2.6.3](#)).
2. Multi-channel, single-time-bin operations – Multiple channels are processed concurrently at a fixed time bin, with no temporal dependency. An example is the common-mode filter (cf. Section [2.6.1](#)).
3. Single-channel, single-time-bin operations – Local transformations are applied to individual samples without inter-channel or temporal references. Examples include pedestal correction and the threshold filter (cf. Section [2.6.2](#)).

A central design challenge was the definition of a data format supporting efficient execution across all three categories. While operations of type (3) are straightforward, types (1) and (2) require conflicting data access patterns—temporal versus spatial—necessitating a flexible yet efficient data representation.

Given the suitability of [FPGAs](#) for highly parallel, streaming-based processing pipelines, the adopted approach maintains continuous data flow through the processing chain, enabling real-time sample modification. The following subsection describes the data format devised to meet these requirements.

## 2.1 Data format of the processing pipeline

The [UL](#) operates at a nominal frequency of 240 MHz, while up to 1600 samples are continuously acquired at 5 MHz. The 1600 new samples per time-bin must be accepted and processed continuously within the corresponding 48 clock cycles. This requirement constrains the sustained processing throughput. The latency between input and output, on the other hand, is not critical, provided that the pipeline can sustain the input rate without data loss.

Data are received over up to 20 optical links, each carrying a maximum of 80 channels. To meet the throughput requirement, at least two samples per clock cycle per link must be processed. With this scheme, all channel data are ingested within 40 cycles, leaving an 8-cycle margin for auxiliary operations such as state management and synchronization.

For efficient, pipelined execution, the data format is designed to be compact and self-contained. Each sample is accompanied by channel-specific parameters—including pedestal and threshold values—and a set of 1-bit flags conveying sample state information. These flags enable localized

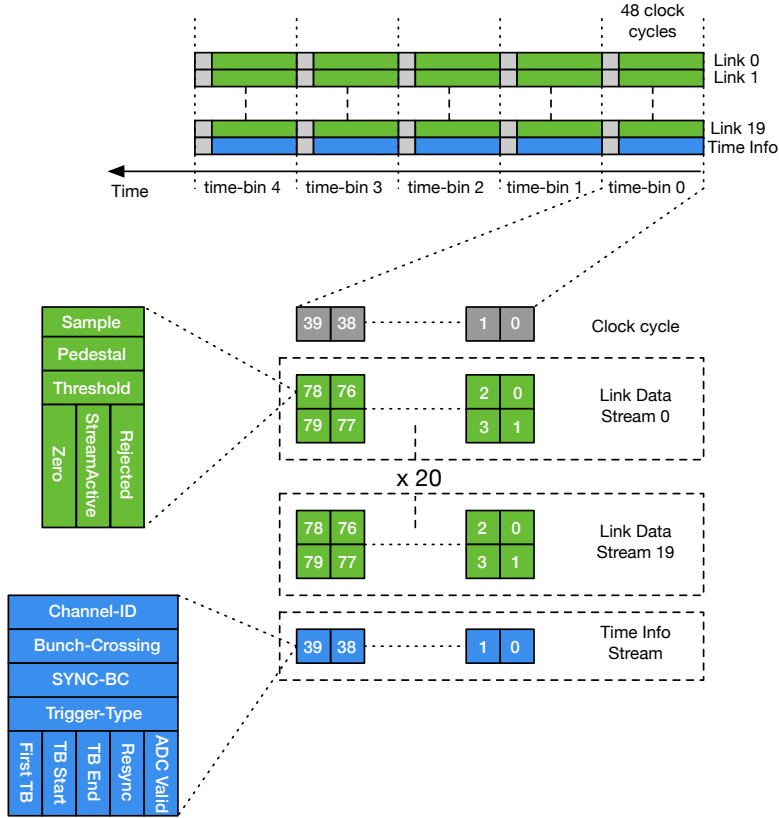


**Figure 4.** Data format of the processing pipeline. All flags and other information are described in the text.

decision-making without requiring access to external context. This dataset consisting of sample value, key parameters and flags is called *link data stream*.

Processing efficiency is further improved through temporal alignment of the 20 link data streams. This alignment renders certain metadata, such as timing information and channel identifiers, common across all streams. Such shared information is extracted and consolidated into a dedicated *time info stream*, which is propagated in parallel with the link data streams throughout processing.

The resulting format ensures that each clock cycle conveys all metadata and control signals necessary for sample processing. Control and steering flags, as well as auxiliary parameters such as pedestal and threshold values, are embedded alongside the sample data to support real-time correction and filtering operations.

Figure 4 illustrates the architecture of this data format. The pipeline comprises 20 link data streams and one time info stream. Each link data stream transmits data for two channels per clock cycle. For each channel, the data includes these three flags:

- *Zero*: Indicates that the sample (after pedestal subtraction) is zero and may be suppressed,
- *StreamActive*: Denotes that the data stream is currently active and synchronized; if a link or an **FEC** is lost, this flag is cleared and the processing logic may react accordingly,

- *Rejected*: Indicates that the sample should not be forwarded to the [FLP](#); however, the sample remains available for internal processing (e.g., ion-tail filter).

The shared time info stream provides global metadata and steering information common to all link data streams, including these flags:

- *Channel-ID*: Identifies which channels are present in the current clock cycle,
- *Bunch-Crossing*: Provides a timestamp corresponding to the [LHC](#) bunch-crossing for the sample,
- *Sync-BC*: Indicates the bunch-crossing number when the most recent *SYNC* pattern was received,
- *Trigger-Type*: Encodes any trigger information associated with the current time-bin,
- *TB Start* and *TB End*: One-bit flags indicating the start and end of a time-bin sample stream, respectively,<sup>13</sup>
- *ADC valid*: Indicates whether valid sample data is present in the current clock cycle (eight of the 48 cycles typically do not contain valid data),
- *First TB*: Marks the first time-bin after the start of a run or a successful re-synchronization (cf. Section 2.5.3); this flag can be used to initialize or reset processing components,
- *Resync*: Signals that the system is currently undergoing re-synchronization (cf. Section 2.5.3), prompting the appropriate handling of incoming data.

This data format enables efficient processing within the [UL](#), supporting all three types of processing operations outlined in the previous section: per-channel temporal filters, per-time-bin spatial filters, and localized single-sample transformations.

## 2.2 Overview of the UL processing pipeline

The [UL](#) design can be functionally divided into three distinct stages: *input stage*, *processing stage*, and *output stage*. A block diagram is shown in Fig. 5.

- The input stage decodes the data from the [GBT](#) frames and generates the link data streams together with the time info stream. It also handles stream synchronization and alignment. A detailed description is given in Section 2.5.
- The processing stage applies the necessary corrections to ensure the desired data quality. It also performs suppression of samples below threshold to reduce the output data volume. Details are provided in Section 2.6.
- The output stage receives the link data streams and the time info stream, extracts the processed samples, and packs them into a dense format for transmission as data blocks. Details are provided in Section 2.7.

---

<sup>13</sup>The start and end could also be inferred from the *Channel-ID*. However, providing explicit flags avoids the need for costly 6-bit comparator logic in each processing module.

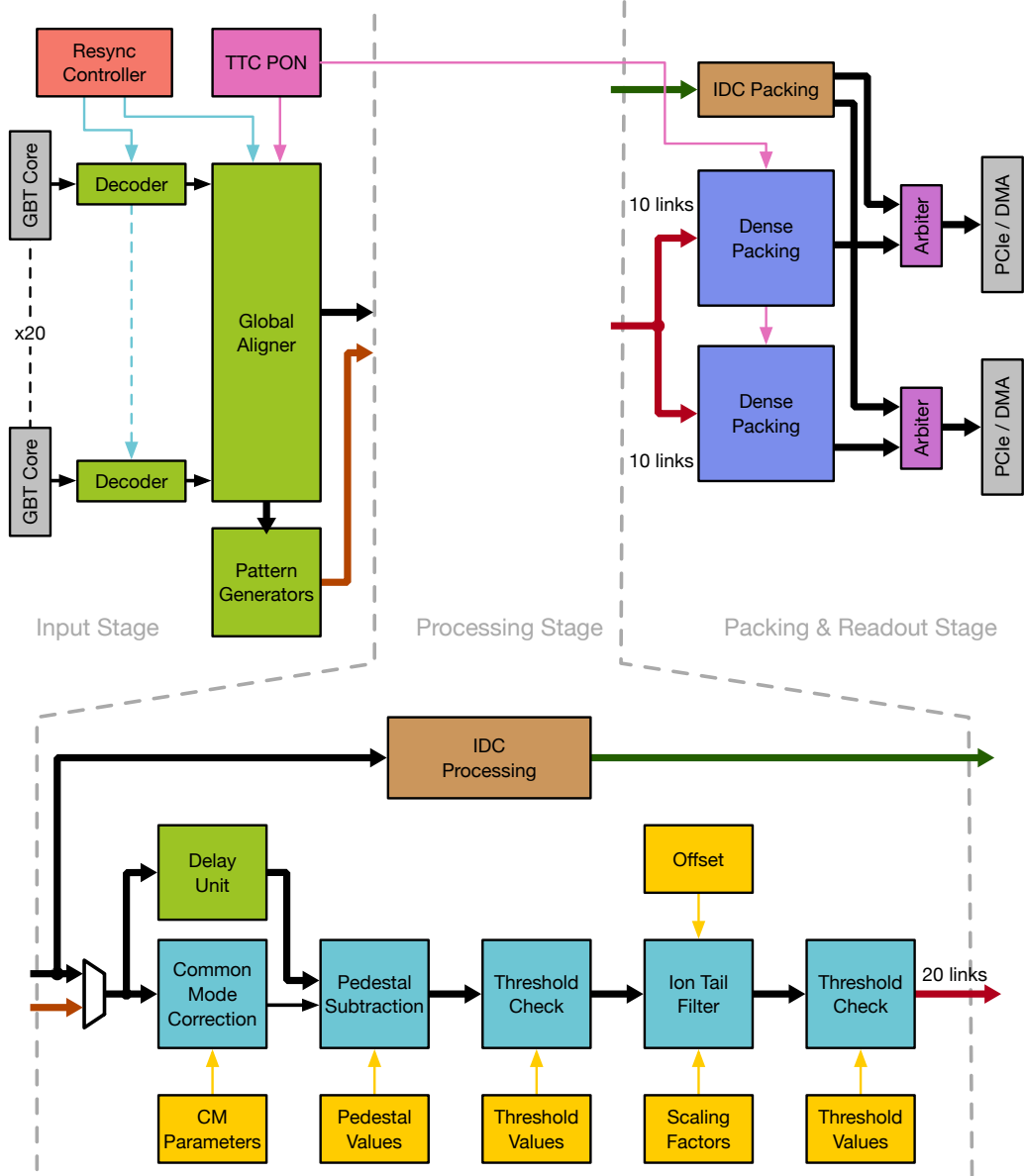


**Figure 5.** Block diagram of the TPC UL.

### 2.3 Slow Control Network (SCN)

The SCN is the configuration and monitoring bus of the UL. It is shown schematically in Fig. 6. It provides internal access to registers and memories for read and write operations. It is implemented as an asynchronous bus with a four-phase (return-to-zero) handshake, enabling safe data transfers between components in different clock domains. In this protocol, the sender issues a request with address and (for writes) data, waits for the receiver's acknowledge, then both sides de-assert their signals to complete the transaction. Although it requires several clock cycles per transfer, standard clock domain crossing (CDC) techniques such as synchronizers ensure robust operation across clock boundaries.

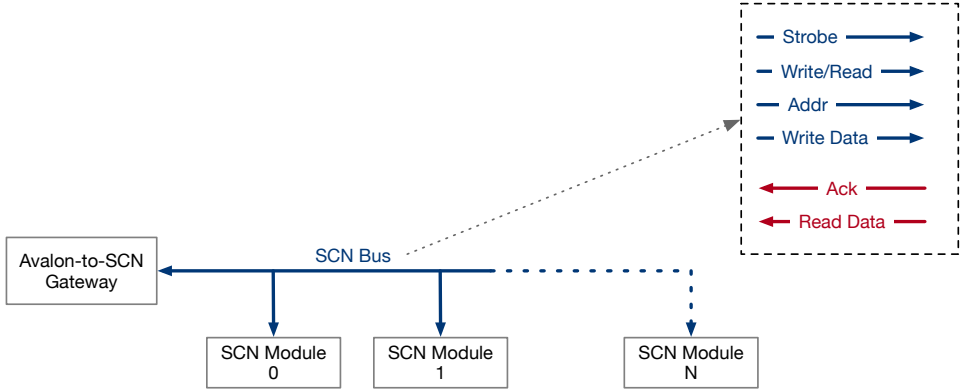


**Figure 6.** Overview of the slow control network (SCN) bus of the [TPC UL](#).

The Common Logic uses Intel’s Avalon bus,<sup>14</sup> but this was considered unnecessarily complex for the [UL](#). Instead, the [UL](#) employs an Avalon-to-SCN gateway that translates between the two protocols.

The SCN address space spans 20 bits, divided into an 8-bit *module* address and a 12-bit *local* address, supporting up to 256 modules with 1024 local addresses each.<sup>15</sup>

## 2.4 Resource utilisation

Table 1 summarizes the available FPGA resources and the utilization achieved by the implemented design on the Intel™ Arria 10 device. The reported metrics include Adaptive Logic Modules (ALMs), which implement combinational and sequential logic; M20K blocks, providing embedded on-chip memory; and DSP blocks, used for high-performance arithmetic operations such as multiplication and accumulation.

The different submodules will be described in the following.

## 2.5 Input stage

The primary responsibilities of the *input stage* are the decoding, synchronization, and alignment of the incoming data. Data are received by the [CRU](#) Common Logic and forwarded to the [UL](#) in the form of [GBT](#) frames, whose payload is detector-specific. For the [TPC](#), eight [GBT](#) frames carry the 80 [ADC](#) samples corresponding to one [ADC](#) sampling clock cycle (i.e., one time-bin), acquired from two and a half SAMPA chips (cf. Sections 1.2 and 1.6).

### 2.5.1 GBT frame decoder

For each optical input link, a dedicated GBT frame decoder (GFD) extracts the samples from the incoming [GBT](#) frames. Since the SAMPA is operated in split mode, each SAMPA provides two data streams and for each link five data streams are received from two and a half SAMPA chips.

<sup>14</sup>The Avalon bus is Intel’s [FPGA](#) interconnect standard, supporting memory-mapped, streaming, and simple signal interfaces.

<sup>15</sup>Avalon addresses are byte-aligned, while SCN addresses are word-aligned; the two least significant bits are ignored.

**Table 1.** Resource utilisation of the Aria10 FPGA.

Module	ALMs	M20K	DSP
Available resources	427.200	2.713	1.518
Resources utilization	303.601	1.424	242
Common Logic	171.109	1.193	0
User Logic	132.492	231	242
UL-Syncbox	6.621	35	0
GBT Frame Decoder	15.905	0	0
Global Aligner	925	20	0
Common-mode correction	28.595	4	22
Pedestal/Threshold memory	599	40	0
Pedestal subtraction and zero suppression	6850	0	20
Ion Tail Filter	18.501	0	200
IDC processor	5997	14	0
Dense packing	26.800	116	0
Misc (Glue logic and monitoring)	21.699	2	0

Each of these streams carries data from a group of 16 SAMPA channels. A single [GBT](#) frame contains ten samples—two from each of the five SAMPA streams.

After initialization or reset, the [GFD](#) locks to the [SYNC](#) pattern to align with the start of the [ADC](#) data stream. Once locked, the SAMPA streams cycle deterministically through the 16 channels, time-bin by time-bin, with the first samples after the [SYNC](#) pattern corresponding to channels 0 and 16 (depending on the connected SAMPA group).

Once the decoder locks to the [SYNC](#) pattern, samples can be reliably decoded and assigned to the correct channel. They are forwarded to the aligner (cf. Section 2.5.2) as an optimized stream, with two samples per [CRU](#) clock cycle. This precursor stream is not yet the final link data stream, as alignment and timing information are still missing.

In parallel, the stream carries the 5 MHz [ADC](#) sampling clock for each SAMPA, oversampled by the 160 MHz [E-link](#) clock (cf. Section 1.2). The decoder monitors the sampling clocks to ensure they remain phase-aligned across all SAMPA chips on the [TPC](#).

### 2.5.2 Global aligner

Since the Tx links from the [FECs](#) to the [CRUs](#) operate with variable, rather than fixed and deterministic latency, the SAMPA [SYNC](#) patterns may arrive at slightly different times on different links. However, the data format described in Section 2.1 requires that samples corresponding to the same time-bin from different links be processed together. This section describes the synchronization and alignment mechanism used to ensure temporal alignment of data streams across all front-end links.

A synchronization trigger from the [CTP](#), received synchronously by all [CRUs](#), initiates the process. The synchronization request is then sent downstream via the [GBTx](#) downlinks to the [FECs](#), ensuring all connected SAMPA receive it simultaneously. They reset, synchronize internally, and begin transmission with the [SYNC](#) pattern, which serves as a time-zero marker, immediately followed by sample data.

As shown in Fig. 7, the [SYNC](#) patterns and subsequent data arrive at the [CRUs](#) at slightly different times due to varying uplink latencies. To address this, the system employs a buffering

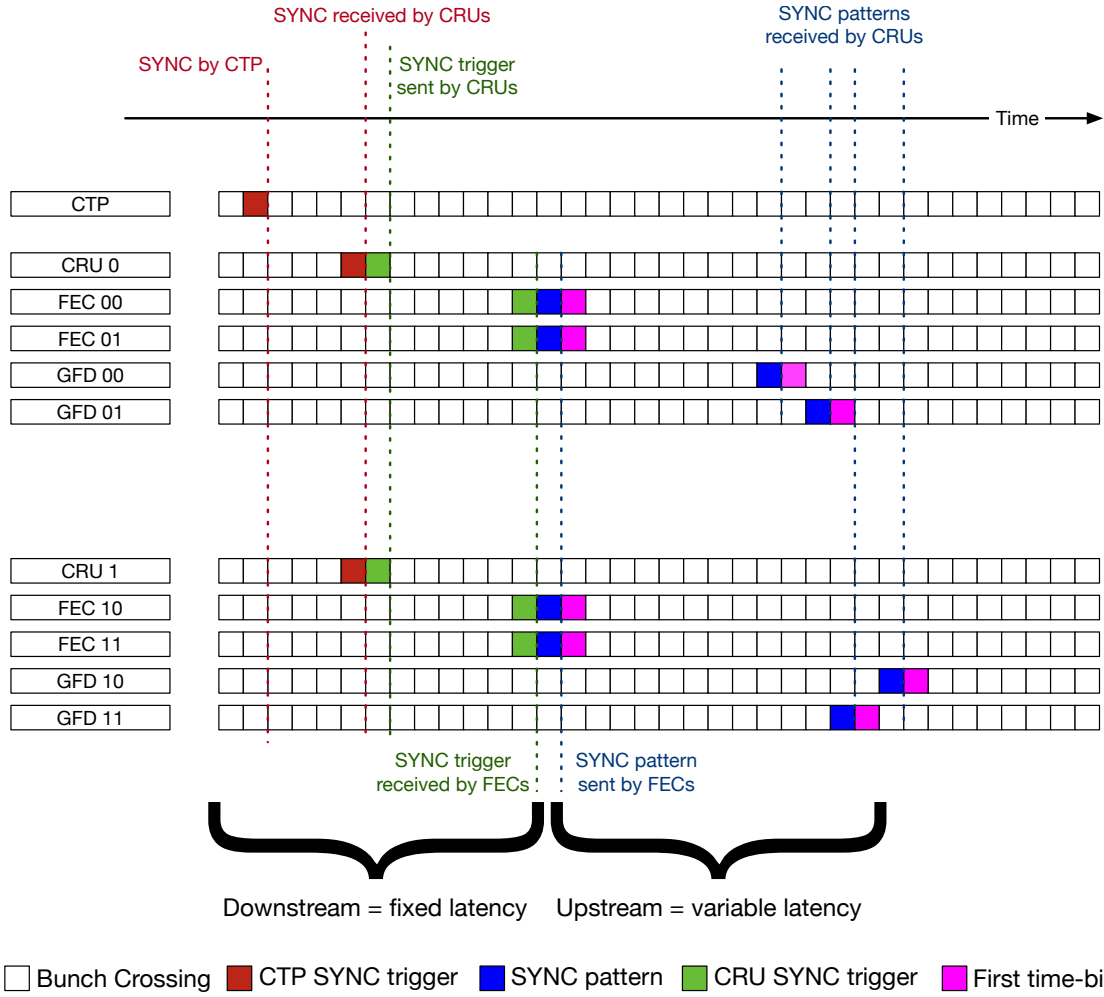


**Figure 7.** Diagram illustrating the synchronization timeline of the [FEE](#). For clarity, only two [CRUs](#) are shown, each connected to two [FECs](#). Within the [CRU](#), the incoming [GBT](#) link data are decoded by the [GFD](#) module.

strategy to ensure temporal alignment before data enters the processing pipeline. This task is handled by the global aligner module.

The aligner takes advantage of the strictly ordered data and the known position of the [SYNC](#) pattern. Alignment then becomes a matter of buffering each input stream in a separate FIFO and reading them out in sync. This is implemented as follows:

- All FIFOs in the global aligner are reset before buffering begins.
- The global aligner receives decoded sample streams from the [GBT](#) frame decoders with the [SYNC](#) pattern already removed, so each stream starts at time-bin 0.
- Each link's data is stored in a dedicated FIFO, preserving the order of samples.
- At a predefined reference time  $t_{\text{align}}$ , all FIFOs are read out simultaneously across all [CRUs](#).

The timing can be modeled as:  $t_{\text{arrival}} = t_{\text{launch}} + t_{\text{roundtrip}}$ , with  $t_{\text{roundtrip}} = t_{\text{down}} + t_{\text{up}} + t_{\delta}$ , where  $t_{\text{launch}}$  is the time the synchronization is triggered in the **CRUs**,  $t_{\text{down}}$  is the propagation delay from **CRUs** to SAMPAs,  $t_{\text{up}}$  is the delay from SAMPAs to **CRUs** and  $t_{\delta}$  represents per-link latency variation due to non-deterministic uplinks. By choosing  $t_{\text{align}} > t_{\text{roundtrip}}^{\max}$ , where  $t_{\text{roundtrip}}^{\max}$  is the maximum observed round-trip time, it is guaranteed that all FIFOs have received some data before starting to read them out.<sup>16</sup>

The global aligner outputs the link data streams and the time info stream described in Section 2.1. It also sets control and synchronization flags, such as *TB Start*, *First TB*, and *Resync*. Both the link data streams and the time info stream are then forwarded to the processing stage (cf. Section 2.6) for further handling.

### 2.5.3 Resync controller

The capability to trigger a re-synchronization ensures that any loss of alignment during data acquisition can be corrected. The re-synchronization sequence for the **GFD** modules and the global aligner is controlled by the resync controller. A resynchronization request originating from the Pattern Player (cf. Section 1.5) in the **CRU** Common Logic is distributed to the **FECs** and to the resync controller.

After a programmable delay  $t_{\text{wait}}$ , the resync controller resets the **GFD** modules. This halts data transmission and places the **GFD** modules in a wait state until the incoming *SYNC* pattern is detected. The value of  $t_{\text{wait}}$  is chosen slightly shorter than the minimum expected round-trip time  $t_{\text{down}} + t_{\text{up}}$  in order to minimize data loss.

During this interval, the global aligner continues reading out its FIFOs. Before the FIFOs are empty, a graceful switchover is performed. The switchover occurs at time-bin boundaries in order to ensure consistency. The aligner continues to emit the link data and time info streams, but replaces all sample values with zeros, allowing the FIFOs to be safely reset without propagating inconsistent data.

Once the **GFD** modules detect the *SYNC* pattern and resume normal operation, the aligner FIFOs begin filling with valid samples again. After the programmable delay  $t_{\text{align}}$ , the aligner returns to standard operation and resumes transmitting the samples.

Throughout the sequence, the link data and time info streams remain continuous and correctly formatted, ensuring full transparency for downstream processing. Zeroing the sample fields guarantees that no invalid data are propagated.

In practice, re-synchronization is performed at fixed intervals (every 10 **TFs**, corresponding to 35 Hz) and is scheduled near the end of the **TF** to minimize its impact on data quality.

### 2.5.4 Pattern generator

The primary objective of the pattern generator is to produce a deterministic data stream that traverses the entire **UL** processing chain, enabling functional validation, particularly of the output stage (cf. Section 2.7).

---

<sup>16</sup>The round-trip times are relatively stable (within a few bunch crossings), and the optimal alignment point was found to be  $t_{\text{align}} = 224$  bunch crossings. Larger values are also valid, provided the FIFO depth can accommodate the additional buffering.

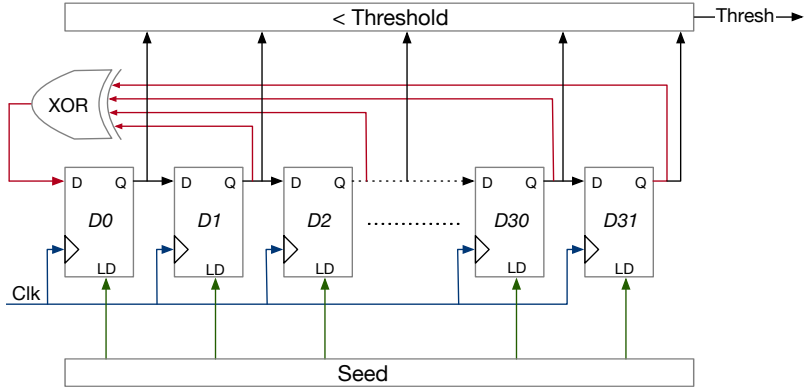


**Figure 8.** The pattern generator core consists of a 32-bit linear feedback shift register with four taps and a seed value which can be loaded. The value held in the register is compared against a programmable threshold. For illustration purposes the taps 0, 1, 30 and 31 are used. In the actual design those vary.

As shown in Fig. 8, the generator uses a 32-bit linear feedback shift register (LFSR), initialized with programmable seed values to generate uniformly distributed pseudo-random numbers. Each number is compared to a configurable threshold, producing a 1-bit flag that determines whether the corresponding sample is zero. If the sample is marked as non-zero, it is replaced with a fixed pattern.

Four fixed pattern modes are supported: a constant value, a channel identifier (*Channel-ID* from the link data stream, cf. Section 2.1), a time-bin counter, or a combination of *Channel-ID* and a reduced time-bin counter. This approach allows simulation of specific occupancy levels and enables embedding metadata, such as time-bin and channel identifiers, directly into the data stream. These embedded markers facilitate software-level verification of data integrity on the **FLPs**. The architecture includes 20 independent pattern generator cores, each assigned to a specific link data stream and individually programmable. To minimize overhead, the design reuses the output of the global aligner as input, modifying only the sample values and associated *Zero* flags in each link data stream.

## 2.6 Processing stage

As shown in Fig. 5, the **TPC UL** processing stage consists of different blocks dedicated to specific tasks in the data pipeline. These blocks operate in real-time, applying corrections and filtering as data streams through the system. The following subsections describe each block’s function, implementation, and role within the overall architecture.

### 2.6.1 Common-mode correction

A *common-mode effect* refers to a baseline shift shared among several (or a group of) detector channels. In the **TPC GEM** system, this effect originates from capacitive coupling between the pad plane and the adjacent GEM foil. It causes all pads beneath a given **GEM** stack to exhibit a common, positive or negative baseline displacement in the presence of signals on the pad plane.

The common-mode signal is characterized by a bipolar waveform: A negative peak coinciding with the induced (positive) signal, followed by an overshoot and a long positive tail. The tail is

approximately exponential, with a time constant defined by the RC circuit formed by the **GEM** electrode’s loading resistor and its capacitance to ground (including the HV cable). While the negative and positive components of the waveform cancel on average under constant occupancy, fluctuations in the signal rate may break this balance. For instance, high-occupancy events—e.g., central heavy-ion collisions—result in positive baseline shifts in subsequent time periods with lower occupancy due to the lingering tails. On the other hand, large energy deposits in the Landau tail can create negative shifts that will not be balanced by prior positive tails.

The baseline variations due to common-mode effect impact zero suppression. Positive shifts may allow noise to pass, increasing data volume and reducing signal fidelity. Negative shifts, on the other hand, reduce—or may even suppress—genuine signals, leading to information loss. Therefore, correcting the common-mode effect prior to zero suppression is essential for maintaining the tracking and particle identification performance of the **TPC**.

A detailed description and discussion of the correction method can be found in [5]. The chosen correction method is the following: The common-mode value is estimated for each time-bin using pads without any physical signal (referred to here as *empty pads*). The value is then subtracted from all samples in the given time-bin.

As shown in Fig. 5, the common-mode correction module is placed upstream of the pedestal subtraction stage. During the computation of the common-mode value, the link data streams and the time-info stream are delayed to maintain temporal alignment. Once computed, the common-mode value is passed to the pedestal subtraction module (cf. Section 2.6.2), where it is added to the samples concurrently with the pedestal subtraction.

To perform the calculation of the common-mode value, the pedestal values must also be subtracted from all samples. The pedestal values are available within the common-mode correction module, as they are included in the link data streams (cf. Section 2.1).

**Pad-by-pad scaling** The capacitive coupling between the pad plane and the adjacent **GEM** foil is not uniform across the detector. Local variations arise from geometrical imperfections, such as wrinkles caused by imperfect foil stretching. These non-uniformities modulate the amplitude of the common-mode signal induced on different pads.

To quantify this effect, dedicated calibration-pulser runs are used. In these runs, a voltage pulse with known amplitude and timing is injected into the **GEM** electrode facing the pad plane, inducing signals on all pads beneath it (cf. [2]). The measured pulser response reflects the local capacitive coupling, and the normalized pulser charge  $k_{\text{pad}}$  provides a relative measure of the per-pad coupling strength. This parameter is used to scale the common-mode correction individually for each pad. Both  $k_{\text{pad}}$  and its inverse  $1/k_{\text{pad}}$  are precomputed and supplied to the **UL** as configuration parameters<sup>17</sup>, ensuring efficient implementation in the **FPGA**.

**Algorithm overview** The common-mode effect impacts all pads under the same **GEM** stack similarly, regardless of whether a physical signal is present. Empty pads contain only the common-mode signal and electronic noise and serve as the basis for estimating the common-mode value for a given time-bin.

---

<sup>17</sup>Divisions are more resource-intensive than multiplications in **FPGAs**; providing both values avoids real-time division and thus improves performance.

The common-mode correction algorithm consists of the following steps:

1. *Empty pad selection and baseline estimation*: Pads are first selected as candidates based on a threshold criterion:

$$q_A < T_1 , \quad (2.1)$$

where  $q_A$  is the sample for the candidate pad and  $T_1$  is the threshold. However, residual signal tails from earlier time-bins can contribute to the pad signal even below this threshold, potentially biasing the empty-pad identification. To mitigate this, a statistical match check is performed:

- For each candidate pad, the sample value, scaled individually using the normalized pulser charge  $k_A$ , is compared to values from ten randomly selected pads, scaled in a similar way,  $q_{(B_n)}/k_{(B_n)}$ , with  $n \in \{0 \dots 9\}$ .
- If the absolute difference is below a programmable match distance  $d_{\text{match}}$ ,

$$\left| \frac{q_A}{k_A} - \frac{q_{(B_n)}}{k_{(B_n)}} \right| < d_{\text{match}} , \quad (2.2)$$

it is counted as a match.

- If the number of matches exceeds a configurable threshold  $N$ , the pad is confirmed as empty.

The common-mode value (CM) for each time-bin is then computed as the average value over all confirmed empty pads.

2. *Pad-by-pad correction*: The corrected sample for each pad is then:

$$q_{\text{pad}}^{\text{corr}} = q_{\text{pad}} - k_{\text{pad}} \cdot \text{CM} . \quad (2.3)$$

Here, the computed value CM is again scaled with the normalized pulser charge in order to account for local variations in capacitive coupling.

As shown in [5], this method ensures robust estimation of the common-mode baseline, even in the presence of overlapping signal tails, and enables accurate pad-by-pad correction tailored to the local detector response.

**Implementation** Although the common-mode correction algorithm is conceptually straightforward in software, its implementation in firmware is considerably more demanding due to stringent timing requirements and the need for extensive loop unrolling and parallel execution.

A top-level overview of the design is shown in Fig. 9. It comprises, for each link data stream, a scaler unit and a compare-and-match unit, as well as a global randomizer unit and the common-mode calculator. The system processes two samples per link data stream and clock cycle, corresponding to 40 samples per cycle across the 20 input links (cf. Section 2.1). The comparison stage constitutes the primary performance bottleneck:  $40 \text{ samples} \times 10 \text{ comparisons} = 400 \text{ parallel comparators}$ . This large number of comparators dominates the resource usage and directly constrains scalability.

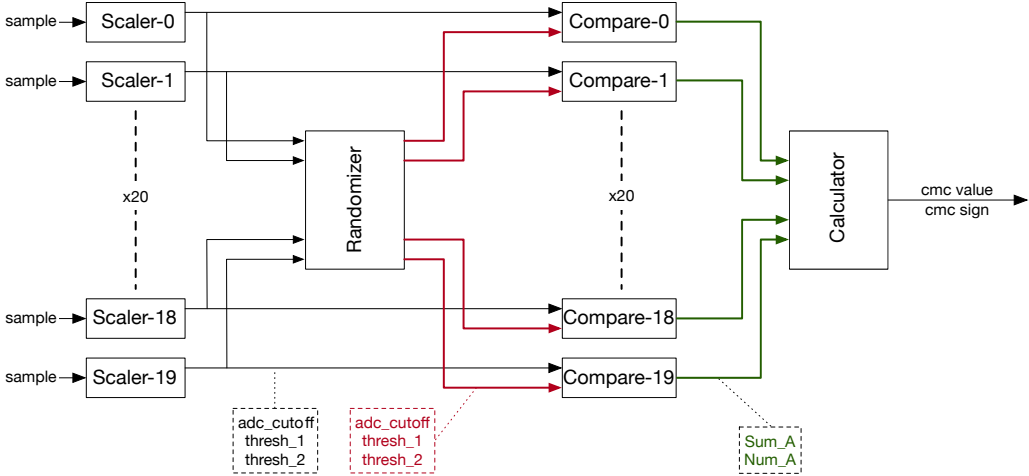


**Figure 9.** Top level overview of the common-mode correction module, consisting of 20 scaler units (one per link), one randomizer unit, 20 compare and match units and the CM calculator. The output of each scaler unit are the clipped sample value and the two flags `thresh_1` and `thresh_2`. The output of the randomizer unit are 10 clipped sample values and the two flags `thresh_1` and `thresh_2` each for each compare unit.

The numerical representation of the input samples is a critical factor in comparator size and speed. A standard 32-bit floating-point format would require large, slow comparators and additional pipelining, further increasing resource consumption. To overcome this, the design employs a custom fixed-point representation optimized for the specific needs of each submodule. Both dynamic range and precision are tuned locally to achieve the required accuracy while minimizing hardware usage.

Fig. 10 provides a detailed view of the modules implementing the individual operations, including the fixed-point precision chosen for each submodule. These components are discussed in the following sections.

The *ADC valid* signal (cf. Section 2.1) is propagated through a dedicated pipeline and used to control the accumulators in the compare-and-match units as well as in the common-mode calculator, ensuring that only valid samples are used. For clarity, this control path is not shown in the corresponding figures.

*Scaler units* The scaler units serve as the pre-processing stage for the calculation of the common-mode value. The arithmetic operations are detailed in Fig. 11.

For each sample, three primary operations are applied: (1) subtraction of the corresponding pedestal value, (2) application of the inverse pad-specific gain factor  $1/k_{\text{pad}}$ , and (3) addition of a fixed offset. The purpose of this offset is to shift the baseline into the positive domain, as the common-mode effect may result in a strong negative baseline displacement. By ensuring that all intermediate values are positive, subsequent processing is simplified.

The scaled values are truncated to comply with the limited range of the common-mode correction algorithm, from  $-100$  to  $+28$ , and are encoded using 7 bits. Consequently, any result exceeding  $T_2 = 28$  is clipped, and the corresponding sample is flagged using the `thresh_2` indicator to denote that it falls outside the valid range.

Additionally, the scaler units perform an early evaluation of the empty-pad pre-selection cri-

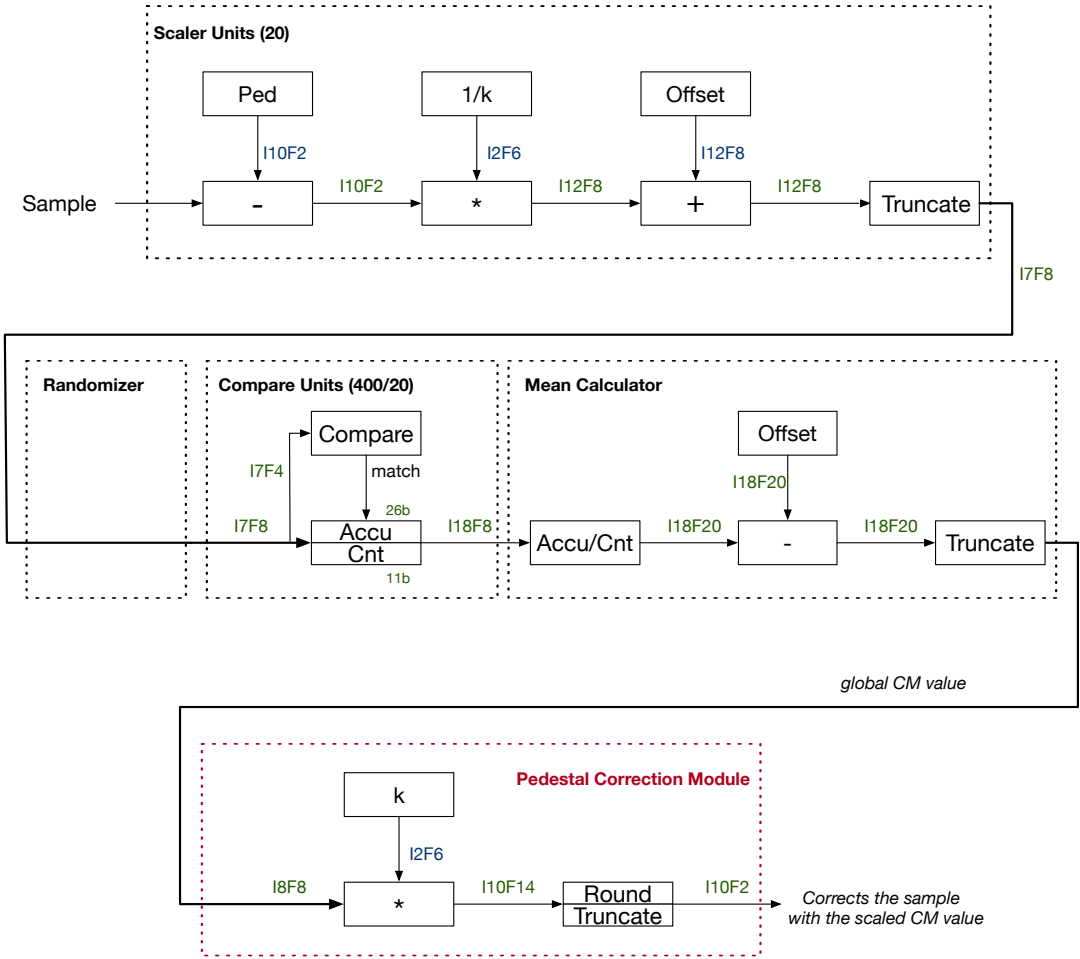


**Figure 10.** Associated fixed-point bit widths for the different arithmetic and logic stages of the common-mode correction pipeline. All calculations use a fixed-point format  $Ix.Fy$ , where  $x$  is the number of bits used for the integer part and  $y$  the number of fractional bits.

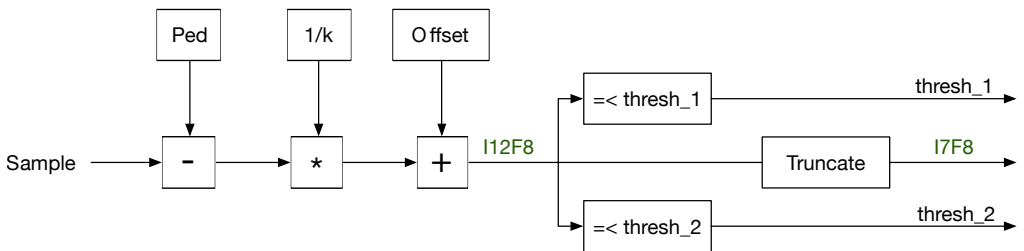


**Figure 11.** Operations of the scaler unit. The necessary threshold checks are performed at this stage in order to reduce the complexity of the subsequent compare units.

terion (2.1) by comparing the scaled charge  $q_{\text{pad}}/k_{\text{pad}}$  to a predefined threshold  $T_1$  (`thresh_1` in Fig. 11), where  $q_{\text{pad}}$  is the value of the sample. Samples below the threshold are flagged using the `thresh_1` indicator. Performing this check at the scaler stage reduces logic complexity and minimizes the number and bit-width of comparators required in the subsequent comparator stage, where ten units operate in parallel.

*Randomizer unit* The Randomizer Unit interfaces between the 20 scaler units and the 20 comparator units. It accepts 20 input data streams and produces 10 distinct output streams per comparator unit, a total of 200 output streams. Despite its name, the randomizer does not perform stochastic or dynamic mapping; rather, it employs a predetermined, fixed selection pattern.

Initially, the architecture was conceived to incorporate true random selection of input streams for each comparator unit. However, this approach was ultimately abandoned due to the excessive logic resource demands associated with implementing randomized selection in hardware. Moreover, the spatial distribution of pads across the scaler units is inherently randomized to a sufficient degree, rendering explicit randomization redundant.

To validate the adequacy of the fixed mapping strategy, a software reference model employing randomized input selection was compared against the fixed-hardware configuration. No statistically significant deviation in performance or behavior was observed, thereby justifying the use of the fixed mapping in the hardware implementation.

*Compare and match units* Figure 12 shows the internal structure of the compare unit, which includes ten match units. The compare unit performs a parallel comparison between an incoming sample  $q_A$  and a set of ten randomly selected reference samples  $q_{(B_n)}$ ,  $n \in \{0 \dots 9\}$ . Each comparison is handled by a dedicated match unit operating concurrently. s

Each match unit checks whether the matching condition (2.2) is fulfilled. To optimize resource usage, the comparison ignores the four least significant bits of the fixed-point representation, as they have negligible impact on the result.

In addition to the amplitude comparison, each match unit enforces two auxiliary conditions: The reference value  $q_{(B_n)}$  must lie within the valid common-mode correction range and must not be clipped. This is indicated by the `thresh_2_B` flag received from the randomizer unit. The candidate value  $q_A$  must also satisfy the pre-selection criterion (2.1) and indicated by the `thresh_1_A` flag. A match is registered only if all three conditions are simultaneously fulfilled.<sup>18</sup>

If the number of matches exceeds a configurable threshold  $N$ , the sample  $q_A$  is classified as originating from an empty pad. It is then included in the calculation of the common-mode value.

An accumulator module keeps track of both the number of valid matches and the sum of the corresponding sample values for each link data stream and time-bin.

*Common-mode calculator* The common-mode calculator (cf. Fig. 13) performs the final computation of the global common-mode value for a given time-bin. It evaluates the mean over all identified empty pads, as determined by the preceding compare and match units.

---

<sup>18</sup>The parameters `thresh_2_A` and `thresh_1_B` are not utilized within this specific match unit; however, in a complementary unit the roles of A and B are interchanged. To ensure a uniform signal pipeline architecture, all four threshold values are consistently supplied regardless of their local usage.

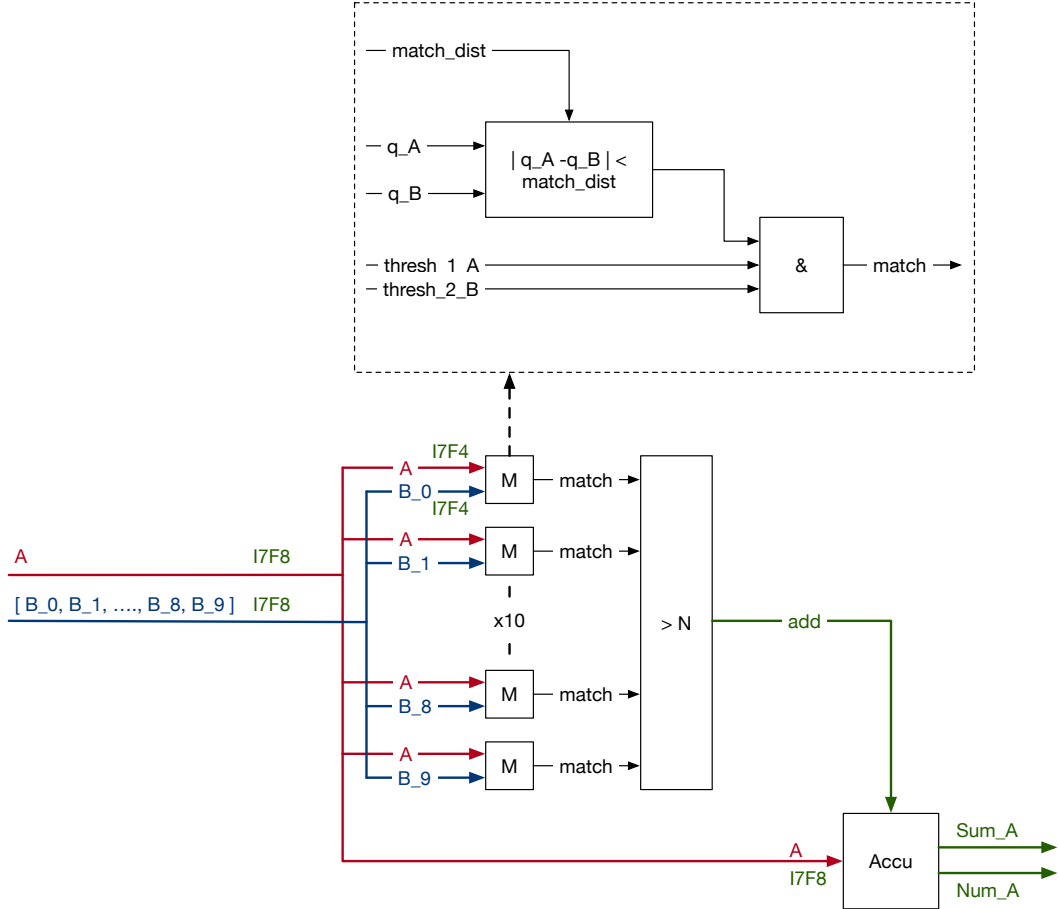


**Figure 12.** Compare unit with 10 parallel match units. Matching is performed at reduced precision (I7F4) to conserve resources, while accumulation is carried out at standard precision (I7F8). The accumulator sums the sample values for all confirmed empty pads ( $Sum_A$ ) and counts the number of empty pads ( $Num_A$ ) for the given time-bin and for the given link data stream.

Due to the high resource and latency cost of division operations in [FPGA](#) implementations, division is intentionally deferred to the final stage. Earlier stages, specifically the compare and match units, output the accumulated charge sum and the corresponding count of empty pads, rather than mean values.

The calculator module aggregates these partial sums and counts from all 20 comparator units to obtain the total accumulated charge and the total number of contributing pads. To meet the stringent 240 MHz timing requirement, this aggregation is performed using a five-stage pipelined adder tree. Each stage consists of registered adders that process intermediate results from the previous stage. Since the tree's full capacity of 32 inputs ( $2^5$ ) is not fully utilized, the structure is asymmetric, and some paths contain pass-through registers instead of arithmetic units.

The outputs of the adder tree (total sum and total count) are subsequently processed by a fully pipelined fixed-point divider. This unit provides a new result every clock cycle after an initial latency

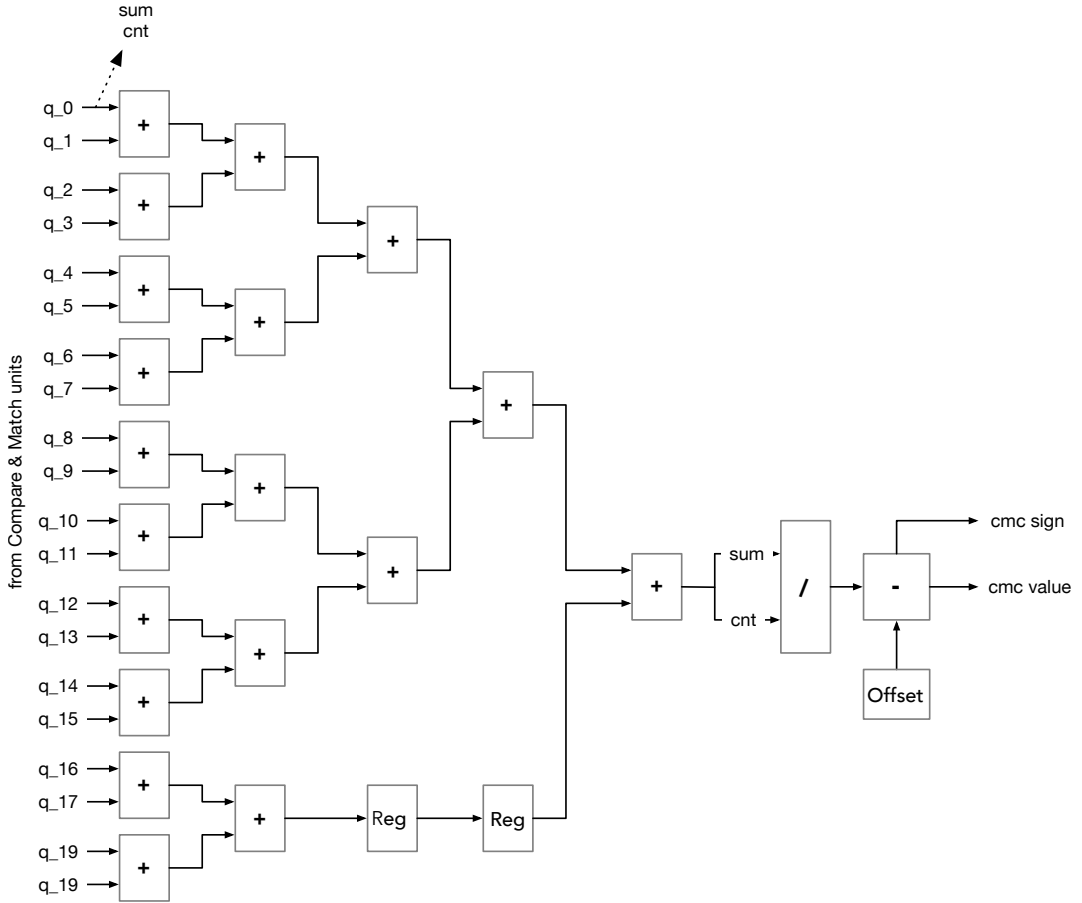


**Figure 13.** The common-mode calculator aggregates the partial sums and match counts from all compare and match units using a five-stage pipelined adder tree. A fixed-point divider then computes the mean, which is subsequently corrected by subtracting the offset introduced by the scaler units, yielding the final common-mode value.

of eight cycles.<sup>19</sup> Finally, the fixed offset introduced earlier by the scaler units is subtracted from the result to yield the true common-mode value. The output consists of the unsigned common-mode magnitude, along with a sign flag indicating the direction of the baseline shift. A valid output is calculated every 48 clock cycles, when all the samples in a time-bin have been processed. This information is then forwarded to the pedestal subtraction and zero-suppression modules (cf. Section 2.6.2), where the actual sample corrections are performed following (2.3).

**Delay unit** A delay unit (cf. Fig. 5), operating in parallel with the common-mode correction module, compensates for its processing latency by delaying the link data streams and the time-info stream. This ensures that the raw samples and the computed global common-mode value reach the pedestal-subtraction and zero-suppression modules in the same clock cycle. Synchronization is maintained using compact embedded FIFOs.

<sup>19</sup>This is the latency of the divider itself.

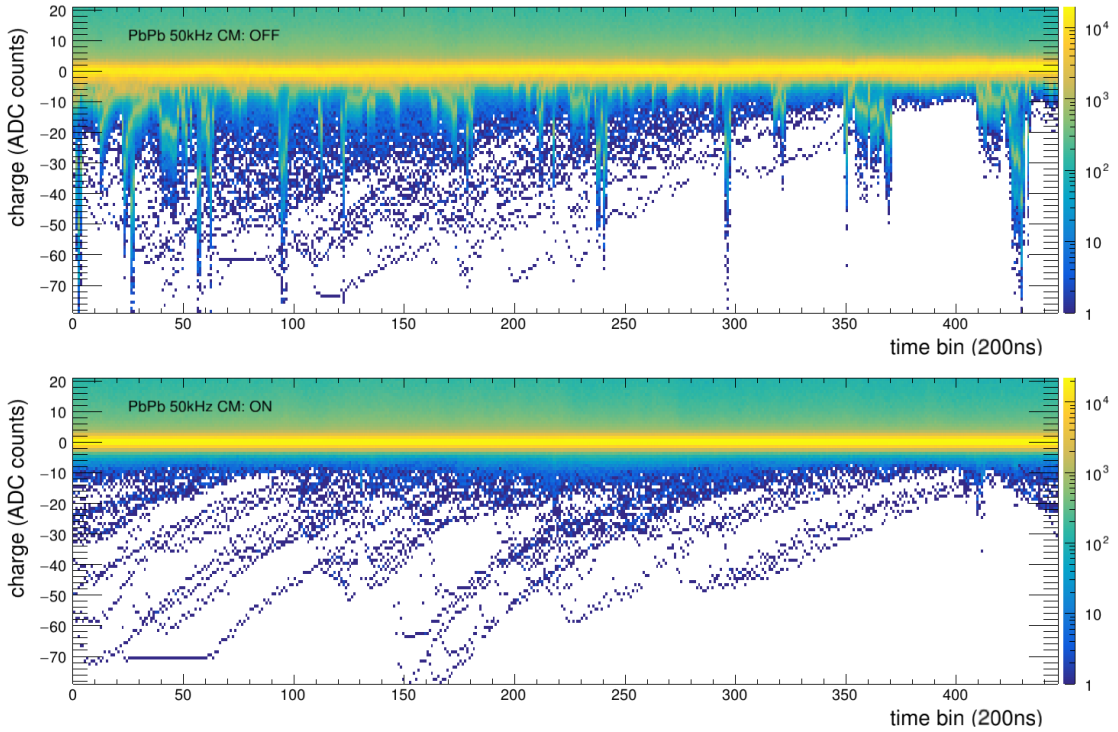


**Figure 14.** Overlay of the data from all channels connected to one [CRU](#) and from many HBF, with common-mode correction disabled (CM OFF, upper panel) and enabled (CM ON, lower panel). The data were recorded in two different runs with Pb–Pb collisions at 50 kHz.

**Performance** The common-mode correction algorithm was validated on the [TPC CRUs](#) using Pb–Pb collisions at 50 kHz. To enable detailed analysis, zero suppression was disabled, allowing the full raw data to be transmitted off-detector. Triggered readout (with a random trigger) was employed in order to reduce the data rate. Multiple data sets were acquired under varying configurations of the common-mode correction module for comparison.<sup>20</sup>

Figure 14 shows an overlay of the data from all channels connected to a single [CRU](#), across many HBF, with common-mode correction disabled (top) and enabled (bottom). The baseline, expected at 0 [ADC](#) counts, is clearly visible in both cases. Without correction, numerous short outliers toward negative [ADC](#) values are observed. These correspond to common-mode signals and can reach amplitudes of several tens of [ADC](#) counts. With correction enabled, these signals are effectively suppressed, and the baseline remains highly stable. The few remaining negative excursions are localized to individual channels and are unrelated to the common-mode effect.

Figure 15 further illustrates the nature of the common-mode signal and the effectiveness of the correction. It plots the correlation between the positive induced signals in a given time-bin and the calculated common-mode value in the same time-bin. When correction is disabled, the expected anti-correlation is observed: large positive signals coincide with increasingly negative common-mode values. The figure also confirms that positive common-mode values can occur,

<sup>20</sup>The figures in this paper are created using the optimum configuration that was found in these tests: threshold  $T_1 = 12$ , match distance  $d_{\text{match}} = 3$ , and number of matches needed to confirm an empty pad  $N = 5$ .

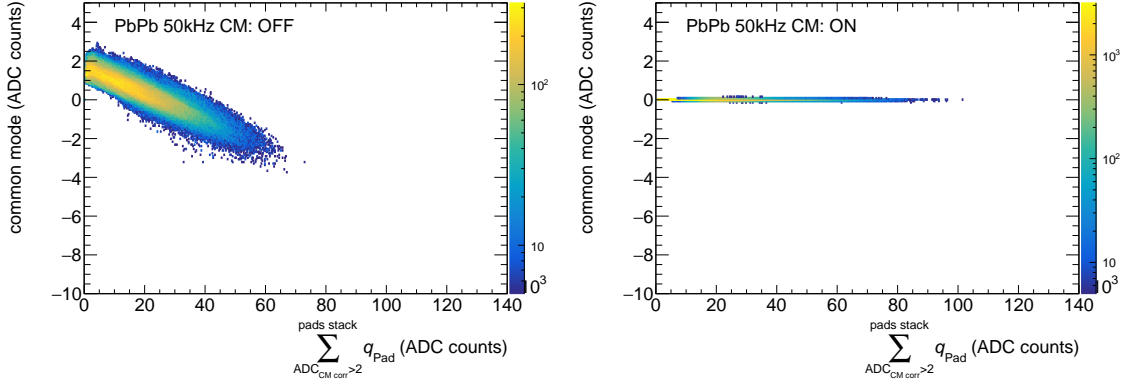


**Figure 15.** Correlation between the sum of all positive signals found in a given time-bin in one [CRU](#) and the calculated common-mode value, with common-mode correction disabled (CM OFF, left panel) and enabled (CM ON, right panel). The data were recorded in two different runs with Pb–Pb collisions at 50 kHz.

highlighting the bipolar nature of the effect. With correction enabled, the described dependence disappears, confirming the removal of all (negative and positive) common-mode contributions.

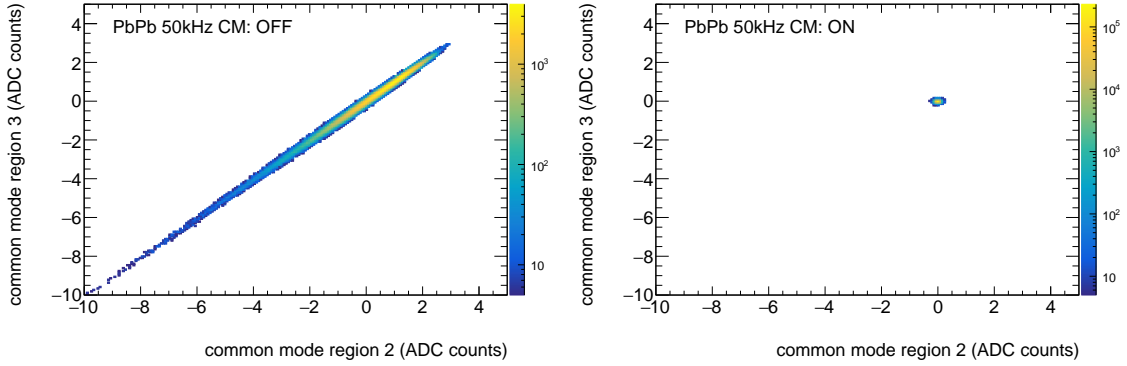


**Figure 16.** Correlation between the calculated common mode values for two [CRUs](#) covering two pad regions under the same [GEM](#) stack, with common-mode correction disabled (CM OFF, left panel) and common-mode correction enabled (CM ON, right panel). The data were recorded in two different runs with Pb–Pb collisions at 50 kHz.

Since all pads under the same [GEM](#) stack are similarly affected by common-mode shifts, and since multiple [CRUs](#) may read out pads from the same stack, the consistency of the correction can be further verified. Figure 16 shows the correlation between the calculated common-mode values from two different [CRUs](#) reading out data from pads under the same [GEM](#) stack. With correction disabled, a strong correlation is observed, reflecting the shared baseline shift. With correction enabled, the correlation vanishes, indicating that the common-mode contribution has been successfully removed independently in each [CRU](#).

These results demonstrate the effectiveness and robustness of the implemented common-mode correction algorithm under high-rate conditions.

### 2.6.2 Pedestal subtraction and zero suppression

Each analog channel of the SAMPA chip exhibits an intrinsic electronic offset—known as the pedestal—which is a stable baseline (in the absence of signals) characteristic of the front-end electronics. This offset biases the sampled [ADC](#) values and must be subtracted to recover the true signal. This operation is performed by dedicated pedestal correction cores. In addition, the common-mode correction is applied to remove the previously calculated baseline shifts shared across multiple channels. Finally, the signal is compared to a defined channel-specific threshold (zero point), with values below this threshold being suppressed.

Each pedestal correction core processes one link data stream and handles two [ADC](#) values in parallel. With 20 independent cores operating concurrently, the system achieves the necessary throughput (1600 samples for 20 links each 40 clock cycles).

Figure 17 shows the processing pipeline. In the first stage, the channel-specific scaling factor  $k_{\text{pad}}$  for common-mode correction (cf. Section 2.6.1) is retrieved from configuration memory. The 6-bit *Channel-ID* from the time info stream is used to address this lookup. In the subsequent stages, each sample undergoes the common-mode adjustment, pedestal subtraction, and suppression of values below threshold. Underflow and overflow protection are applied, matching the [ADC](#)'s dynamic range (0 to 1023). A debug mode can redirect selected [ADC](#) channels to output the common-mode value instead of the sample values, aiding diagnostics and calibration. The pipeline relies on fixed delays to keep all data streams and correction parameters precisely aligned in time, ensuring each sample is processed with its matching common-mode and pedestal values. Consequently, minor delay elements, implemented as registers or shift registers, are inserted as required to ensure proper timing alignment.

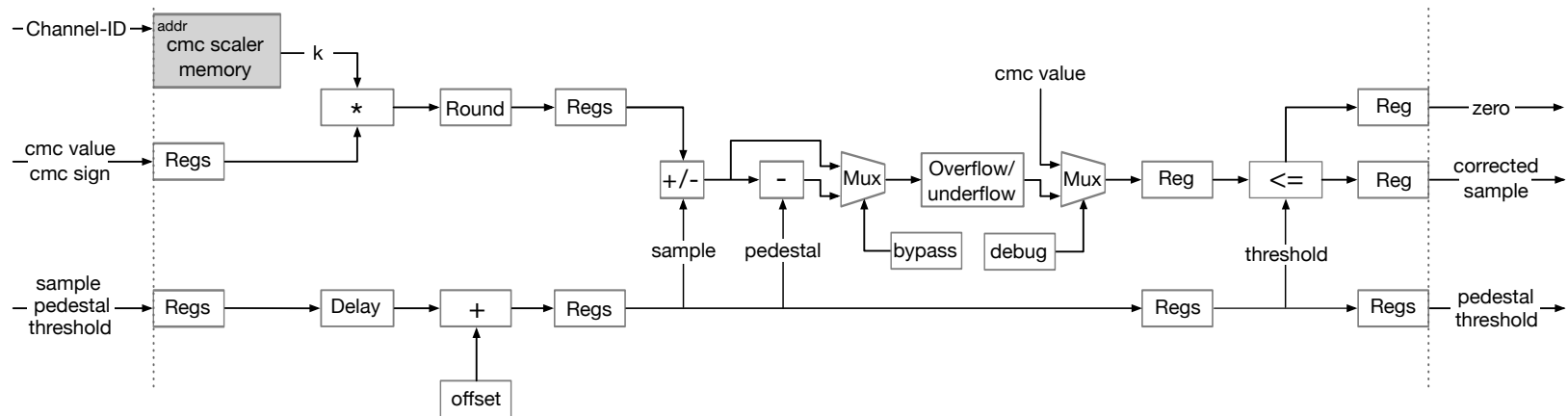


**Figure 17.** Overview of the pedestal correction core. The *Channel-ID* from the time info stream is used to address the lookup of the scaling factor  $k_{\text{pad}}$  for the application of the common-mode correction in the first stage. The module outputs the corrected sample and the *Zero* flag used in the link data stream to indicate that the sample is below threshold and may be suppressed.

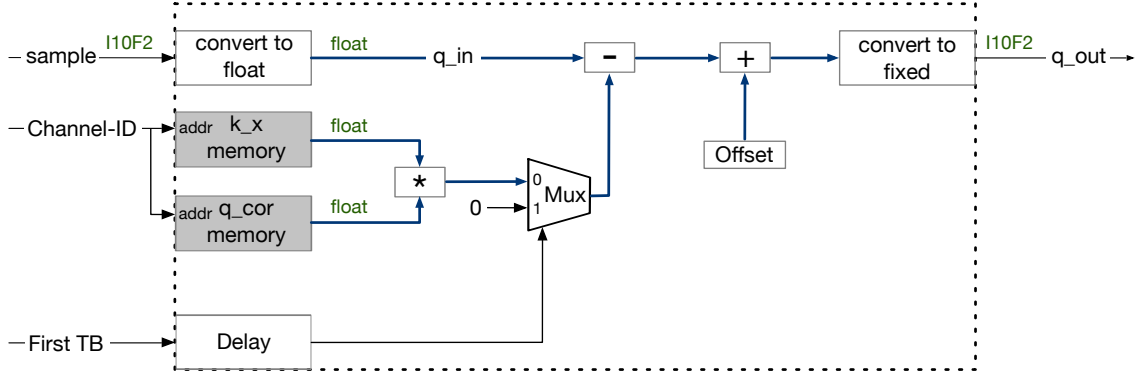


**Figure 18.** Correction algorithm of an ion-tail filter core. The scaling factor  $k_x$  and the correction value  $q_{\text{cor}}$  are fetched from memory using the *Channel-ID*. Correction of the first sample in a sequence is inhibited using the *First TB* signal, as no valid correction value is available at that point. Both signals are available from the time info stream. The *First TB* signal is delayed by four clock cycles using a shift register while the sample is converted to single-precision floating-point format, which is used for all computations inside the dashed box.

### 2.6.3 Ion-tail filter

The ion-tail filter is a digital signal processing algorithm designed to mitigate characteristic signal distortions caused by slowly drifting ions generated in the induction gap of the [GEM](#) stack [5]. These ions induce an exponentially decaying tail in the pulse shape, which degrades signal quality and, if uncorrected, impacts subsequent data processing and reconstruction.

Two main sources of ion-induced distortion can be identified: (i) ions generated in the high-field region near the [GEM](#) holes, just below the final [GEM](#) amplification stage—an effect common to all [GEM](#)-based systems; and (ii) ions produced throughout the full induction gap as a result of charge amplification along its volume—an effect specific to the high-voltage configuration used in the [ALICE TPC](#).

**Algorithm overview** The ion-tail filter is implemented as a recursive Infinite Impulse Response (IIR) filter designed to model an exponential decay. It operates independently on each input channel, iterating over the incoming samples. At each iteration, the input sample  $q_{\text{in}}$  is adjusted using a scaled correction term  $q_{\text{cor}}$ , yielding the filtered output  $q_{\text{out}}$  as:

$$q_{\text{out}} = q_{\text{in}} - k_1 \cdot (1 - k_2) \cdot q_{\text{cor}} = q_{\text{in}} - k_x \cdot q_{\text{cor}}. \quad (2.4)$$

Concurrently, the correction factor  $q_{\text{cor}}$  is updated for use in the subsequent iteration according to the recursive relation:

$$q_{\text{cor}} = k_2 \cdot (q_{\text{in}} + q_{\text{cor}}). \quad (2.5)$$

The filter behavior—specifically, the degree of smoothing and the strength of the feedback—is governed by the parameters  $k_1$  and  $k_2$ . To reduce resource usage and avoid redundant computations in the [FPGA](#) implementation, the coefficient  $k_x = k_1 \cdot (1 - k_2)$  is precomputed and stored as configuration parameter together with  $k_2$ .

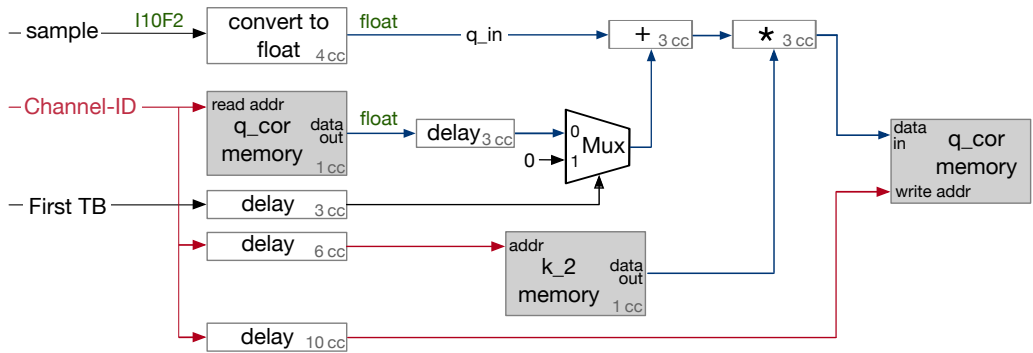


**Figure 19.** Dual-port RAM is used to store the correction factor  $q_{\text{cor}}$ . The chosen architecture supports concurrent read and write operations, enabling iterative updates of  $q_{\text{cor}}$ . The coefficients  $q_{\text{cor}}$  and  $k_2$  are retrieved from memory using the *Channel-ID*. The value of  $q_{\text{cor}}$  is forced to zero for the first time-bin in a sequence. The sample is converted to single-precision floating-point format to improve numerical accuracy in the subsequent calculations. The diagram also indicates the latencies of the individual operations in clock cycles (cc).

**Implementation** Although the ion-tail correction algorithm is relatively straightforward to implement in both software and firmware, the primary challenge arises from the high channel count (up to 1600 channels) and the stringent timing constraint of 48 clock cycles. This requirement necessitates the simultaneous processing of 40 channels in parallel. Additionally, higher numerical precision than the native 12-bit fixed-point format is desirable to maintain computational accuracy throughout the correction process. To address this, all 12-bit input samples are first converted to 32-bit floating-point representations. All arithmetic operations are performed in floating-point, and the final result is subsequently converted back to a 12-bit fixed-point integer format.

**Ion-tail filter core** The ion-tail filter is implemented using 40 dedicated filter cores, each operating in parallel. Two cores are assigned to each link data stream: one handles even-numbered channels, and the other processes odd-numbered channels, with each core managing 40 channels concurrently. The correction logic of an individual core is depicted in Fig. 18. Upon receiving a sample, the core converts it into a floating-point value. Simultaneously, the *Channel-ID* from the time info stream is used to retrieve the correction factor  $q_{\text{cor}}$  and scaling factor  $k_x$  for the given channel from memory. The scaled correction is computed as the product of the correction and scaling values and is then subtracted from the floating-point representation of the input sample, following (2.4).

For testing and debugging purposes, a configurable offset can be applied after the correction and before converting the result back to fixed-point format. In the case of the first sample in a sequence, where no valid correction factor exists, the scaled correction term can be effectively bypassed by forcing its value to zero via a multiplexer connected to the delay unit.

The processing pipeline is fully unrolled into 13 sequential stages without internal feedback loops, enabling a throughput of one sample per clock cycle and a fixed latency of 13 clock cycles.

*Correction factor update* Figure 19 illustrates the logic responsible for the iterative update of the correction factor  $q_{\text{cor}}$  following (2.5). At the core of the design is a dual-port memory, which stores

the current values of  $q_{\text{cor}}$  for all 40 channels. This memory architecture enables concurrent read and write operations through dedicated ports, facilitating efficient real-time updates.

During each processing cycle, the input sample is converted to a 32-bit floating-point value  $q_{\text{in}}$ , while the corresponding  $q_{\text{cor}}$  value is simultaneously retrieved from memory. To compensate for the latency introduced by the floating-point conversion, the  $q_{\text{cor}}$  value is delayed by three clock cycles. The updated correction value is then computed by summing  $q_{\text{in}}$  and  $q_{\text{cor}}$ , followed by multiplication with the filter coefficient  $k_2$ , following (2.5). The resulting value is subsequently written back to memory via the write port.

The update is not executed when *ADC valid* in the time info stream indicates that no valid sample data is present in the current clock cycle (cf. Section 2.1). This is not shown in Fig. 19.

The update logic is highly pipelined and optimized for resource efficiency. Rather than delaying the 32-bit coefficient  $k_2$  through each pipeline stage, the design instead delays the 6-bit channel address, significantly reducing register usage. This approach yields substantial resource savings.<sup>21</sup> This optimization is applicable only to  $k_2$ ; the  $q_{\text{cor}}$  values themselves cannot be delayed in this manner, as they are also required without latency in the correction stage.

Further resource savings are achieved by utilizing small, embedded memory blocks to store  $q_{\text{cor}}$  values, rather than conventional register arrays. A register-based implementation would require 51 200 registers<sup>22</sup> in addition to logic for address decoding and control. By leveraging embedded memory, these overheads are eliminated, enabling a compact and efficient hardware implementation.

#### 2.6.4 Integrated digital currents

The integrated digital currents (IDCs) are the cumulative sums (integrals) of raw *ADC* samples from a given channel over a defined time window. This quantity forms part of the calibration procedures and is used to correct distortions from space charge in the drift volume. Within the *UL* processing framework, the *IDC* processor implements the functionality of calculating the *IDCs* in parallel with the primary raw-data pipeline (cf. Fig. 5).

As shown in Fig. 20, the *IDC* processor consists of three principal components: the *link core*, the *controller* and the *packetizer*. The link cores integrate incoming samples; 20 cores operate in parallel to cover up to 1600 channels, each producing 80 per-channel sums. These results are forwarded to the packetizer, which formats the data into packets for Direct Memory Access (DMA) transfer.

The controller acts as the central coordinator. It governs integration timing using external inputs such as orbit and bunch-crossing (BC) signals or trigger events, configures the integration windows for the link cores, and signals the packetizers when accumulated data is ready for transmission.

The *IDC* processor uses a dedicated packet format and an independent transmission channel, allowing *IDC* data to be processed separately and asynchronously by the online farm, without interfering with the main data stream.

The link core is the most resource-intensive *IDC* processor component, owing to 20 parallel instances, each maintaining integrated sums for 80 channels. Its optimization is key to efficient FPGA resource usage. The core's operation is shown in Fig. 21.

<sup>21</sup>The savings amount to  $(32-6)$  bits  $\times$  6 pipeline stages  $\times$  40 cores = 6240 registers (0.5 % of all available Flip-Flops).

<sup>22</sup>1600 channels  $\times$  32 bits = 51200 registers (4 % of all available Flip-Flops).

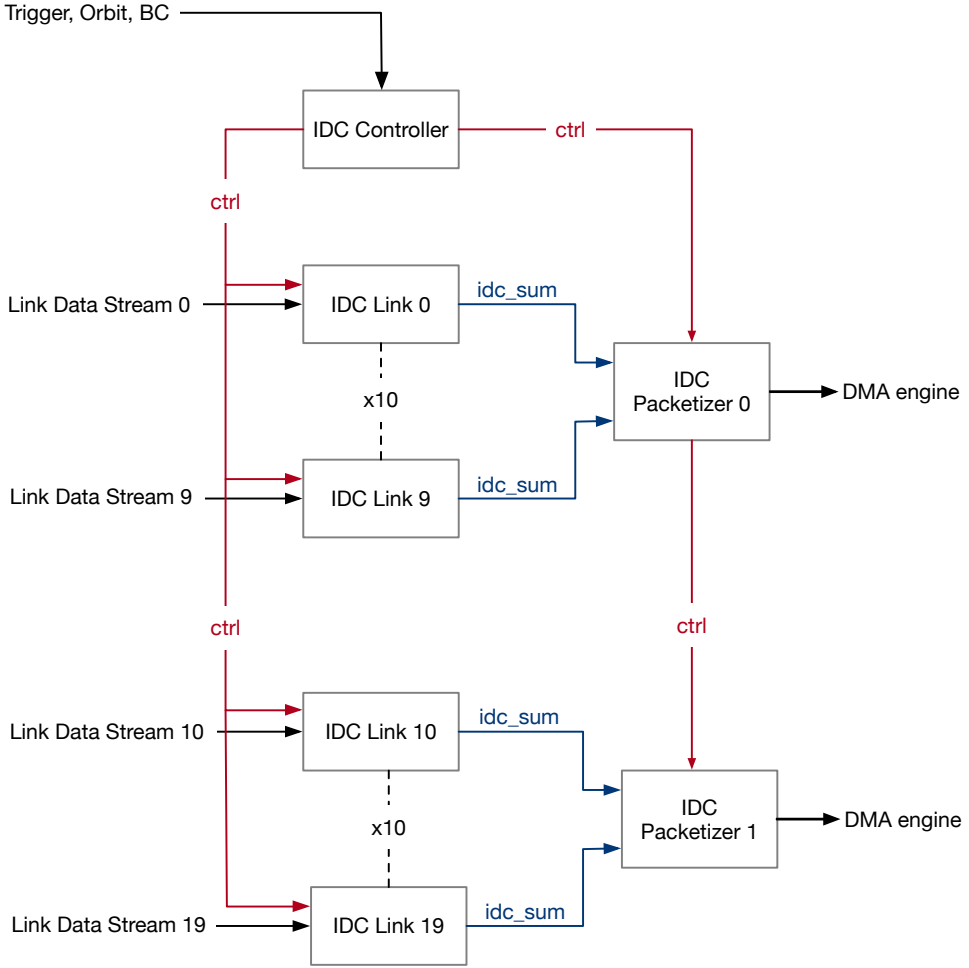


**Figure 20.** IDC processor. The link cores integrate the incoming samples, while the packetizer formats the data into packets. All operations are coordinated by the controller.

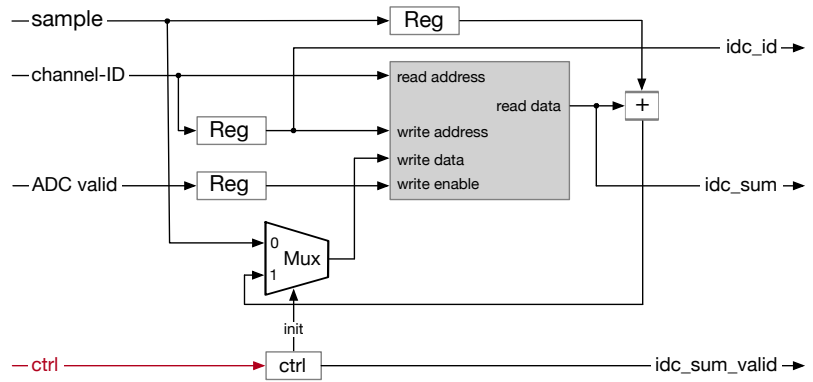


**Figure 21.** The IDC link core. It consists of a dual-port memory that enables simultaneous read and write operations. New samples are added to the stored value, and the updated sum is written back in the next cycle.

A small dual-port memory enables simultaneous read/write. In accumulation phases, each new sample is added to the stored value read from memory, and the updated sum is written back in the next cycle.

At the end of an integration period, the initialization phase is reused to sequentially read out the accumulated sums while simultaneously storing new samples. This interleaved pattern enables continuous integration and readout without buffering pauses, maintaining high-throughput and deterministic performance.

## 2.7 Output stage

The output stage receives the link data streams and the time info stream, extracts the corrected samples, and packs them into a dense, zero-suppressed format. The goal is to generate compact data blocks with minimal padding and size-optimized headers, with the aim to significantly reduce the total [TPC](#) output data volume, keeping it well below  $1 \text{ TB s}^{-1}$ , as required by the bandwidth constraints of the downstream processing stages.

[ALICE](#)’s readout framework mandates that the detector data corresponding to a single [HBF](#) be encapsulated into one or more contiguous packets, each with a maximum size of 8 KiB. To meet this requirement, each of the two dense packing instances (cf. Fig. 5) is capable of producing correctly formatted packets from up to 10 detector links operating at full data rate. The packet format has been optimized for efficient parallel processing on [GPUs](#) within the [EPN](#) farm.

### 2.7.1 Data format

The produced packets conform to [ALICE](#) readout requirements, specifically: each packet is at most 8 KiB in size and begins with a Raw Data Header (RDH) [11, 12]. The payload is structured as a sequence of time-bin blocks. Each block begins with a byte-aligned block header that includes the number of contributing links and the bunch-crossing identifier. Following the block header, link headers are included for each active link. These headers are then followed by the data payloads corresponding to each active link.

Per detector link and time-bin, up to 80 extended 12-bit samples can arrive at the input of the Dense Packing unit. To efficiently identify which samples are included in a payload, the link headers implement a compact two-level bitmask scheme.<sup>23</sup> The scheme incorporates a header bit that specifies whether the bit mask is static or dynamic. In the static configuration, the bit mask is fixed and comprises 80 bits, each representing the presence or absence of a corresponding sample. In the dynamic configuration, the 80 samples are partitioned into ten groups of eight samples, and a 10-bit mask is used to indicate the presence or absence of each group.

Zero-valued samples are suppressed, and the remaining non-zero 12-bit samples are densely packed without regard to byte boundaries.<sup>24</sup> Each packet may contain zero or more partial or complete time-bin blocks. To minimize packet overhead, packets are filled to the maximum size whenever possible. Consequently, a single time-bin block may be split across consecutive packets

---

<sup>23</sup>The time-bin block header has a fixed size of 2 B. Link header sizes range between 3 B and 10 B, depending on the number of active channels. The maximum size of a link data payload is  $80 \times 12 \text{ bit} = 120 \text{ B}$ . Thus, the maximum size of a time-bin block is  $2 \text{ B} + 10 \times 10 \text{ B} + 10 \times 120 \text{ B} = 1302 \text{ B}$ .

<sup>24</sup>Only at the end of a time-bin block may a 4-bit padding be added to ensure byte alignment for the next block.

within a **HBF** when approaching the 8 KiB size limit. Only the first packet of a **HBF** is guaranteed to begin with a full time-bin block.

Depending on the channel activity, the number of packets per **HBF** varies from as few as one (in the case of no activity) up to 72 for full-channel activity. Each packet ends with a 128-bit meta word that contains metadata including the number of time-bins in the packet, the number of samples, and the offset of the first time-bin block within the packet. This meta word enables precise access to time-bins within each packet and facilitates the correct time-wise alignment and distribution of data across different **STFs** to the **GPUs** for reconstruction.

Additionally, the final packet of each **HBF** includes a 128-bit trigger word positioned immediately before the meta word. This word provides information about the types and timing of all triggers received during the **HBF**.

### 2.7.2 Merging and packing pipeline

Figure 22 illustrates the architecture of the dense packing pipeline. The pipeline’s first three stages operate on a time-bin basis and progressively merge data into wider data words until the target output width of 256 bit is achieved. The later stages wrap the resulting stream of time-bins with an **RDH**, along with meta and trigger words, to form 8 KiB packets ready for transmission. The operation of all pipeline components is coordinated by a central layout calculation unit.

At Stage 0, ten parallel instances—one per link data stream—pack the incoming corrected 12-bit samples into dense 64-bit words. These words are written to FIFOs that serve as inter-stage buffers. Depending on the number of non-zero samples in a given time-bin, each Stage 0 unit generates between 1 and 15 words. All words, except potentially the last, are fully populated with samples; the final word may be zero-padded.

Once a Stage 0 unit finishes processing a time-bin, the number of non-zero samples per link is known. Based on this and the end position of the previous time-bin, the layout calculation unit determines the sizes and start positions for each link’s payload and header in the current time-bin block. It also accumulates metadata for the meta word and maintains overall packet layout throughout the **HBF**, ensuring correct placement of **RDH**, placeholder regions, and final metadata.

The data merging scheme relies on computing the current position and contribution size for each time-bin, and precalculating the target positions for subsequent stages. Stream widths expand from 64 bit in Stage 0 to 128 bit in Stage 1 and 256 bit in Stage 2. As merging is performed in parallel, each stream is shifted to its designated position and zero-padded at both ends, enabling seamless concatenation by applying a logical *OR* between adjacent streams.

Stage 1 comprises one header generation unit and five regular merging units. The header unit produces the time-bin block header and link headers, while each merger processes data from two Stage 0 instances.

All Stage 1 units follow a common operational scheme: The unit controllers use barrel shifters to align incoming 64-bit data words to the positions specified by the layout unit. These aligned words are written into asymmetric FIFOs with 64-bit input and 128-bit output width, acting as buffers toward Stage 2. To maintain correct alignment at the 128-bit level, zero-padding may be inserted before the first and after the last data words.

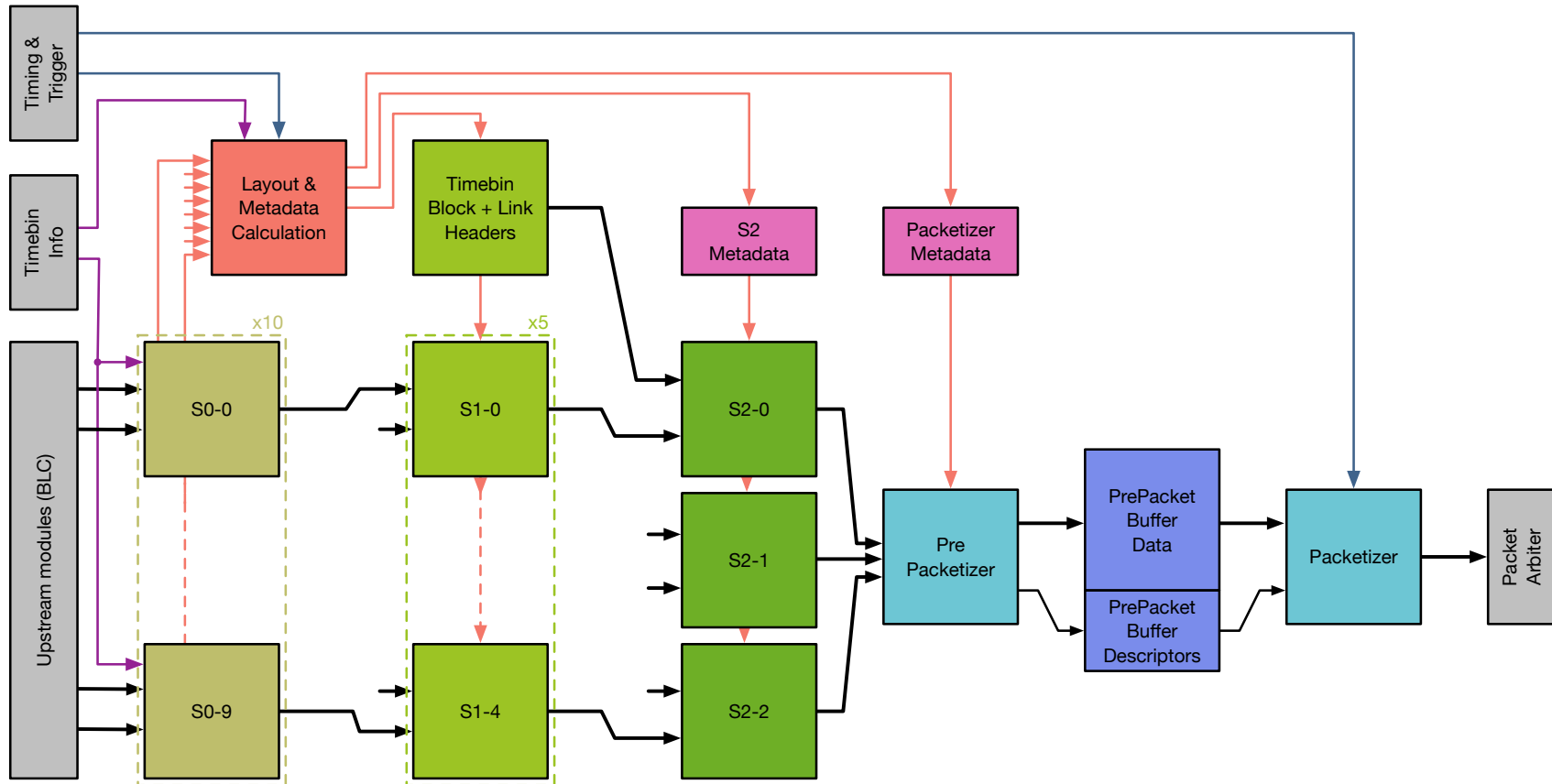


**Figure 22.** Simplified overview of the pipeline packing the data of up to 10 link data streams into one or more densely packed packets of up to 8 KiB.

At Stage 2, the pipeline merges prealigned and padded 128-bit words into wider 256-bit words using asymmetric FIFOs (128-bit in / 256-bit out). These units also insert placeholders for the meta and trigger words at predefined positions. Thanks to the alignment information provided by the layout unit, all Stage 1 and Stage 2 components can operate in parallel and complete the packing of a single time-bin within the available 48 clock cycles at 240 MHz.

The prepacketizer merges the output from the three Stage 2 units and replaces the previously inserted placeholders with actual meta and trigger data collected by the layout unit. Whereas the earlier stages operate on time-bins, the prepacketizer outputs prepackets—complete packet structures except for the **RDH**—along with a prepacket descriptor. This descriptor is then passed to the packetizer, which uses its contents to generate the final **RDH**. It then assembles and transmits full packets in 256-bit words to the Common Logic, which handles forwarding to the **FLP**.

### 3 User Logic for auxiliary systems

The **TPC** includes several auxiliary systems designed to provide stimuli and additional data to ensure correct operation and enhance calibration. A key requirement for these systems is that their operation must be synchronized with the sampling clock of the SAMPAs and the TPC data readout. Given its interface with the experiment’s trigger and timing system, and its use of the **GBT** communication channel with fixed latency, the **CRU** is well suited to implement the necessary control and readout logic for these auxiliary systems. Figure 23 presents a simplified overview of the Synchronisation Box (SyncBox) **UL**, which is responsible for controlling the laser and pulser systems and managing the readout of the High Voltage Current Monitor (HVCM) systems.

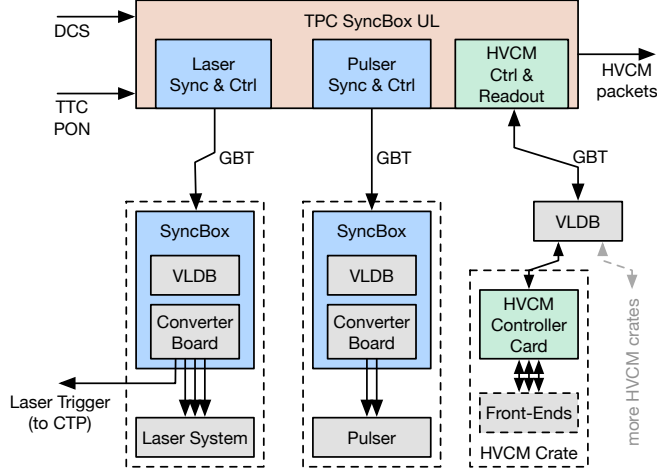


**Figure 23.** Building blocks of the Synchronisation Box (SyncBox) **UL** and interfaces to the external systems.

To enable control of the laser and pulser systems via the **GBT**, several **SyncBoxes** were developed. Each **SyncBox** consists of a Versatile Link Demonstrator Board (VLDB) [13], equipped with a **VTRx** and **GBTx**, and a custom-designed interface board. The **VLDB** forwards the **GBT** downlink signals received via its **E-link** to the interface board with deterministic latency. There, the signals are converted into optical and electrical outputs at the required levels. All logic required to generate properly timed and synchronized control signals is implemented within the **CRU**.

### 3.1 Laser control

Pulsed UV lasers [14] are used to simulate ionizing tracks within the active volume of the **TPC**, supporting alignment, calibration, and drift time monitoring studies.

The converter board provides five output signals<sup>25</sup> for each of the two lasers. These outputs are controlled by two independent laser controller instances implemented within the **SyncBox UL**.

For accurate data analysis, it is essential to synchronize the firing of the laser with the sampling clock of the SAMPAs. Additionally, aligning the laser operation with the **TFs** (cf. Section 1.1) helps define precise time positions in the data stream where laser events are expected.

The controller logic in the **CRU** generates a periodic signal to indicate valid time windows during which a laser sequence may be initiated. This signal has a frequency of approximately 10 Hz, determined by the fixed repetition rate of the lasers. The associated counter operates synchronously with the **LHC** clock and is reset using the same trigger signal as the SAMPAs. The system is configured such that the start signal frequency is an even integer multiple of the **TF** frequency, ensuring synchronization with both the sampling clock and the readout.

Embedding laser events in regular data-taking with collisions enables correction of drift velocity variations across space and time. To support this, the laser controller sends a trigger to the **CTP**, allowing the readout **CRUs** to tag data packets containing laser events.

The timing and duration of each laser output signal are fully configurable relative to the start signal. This flexibility accommodates the hardware requirements of the laser system and allows laser events to be positioned well within a **TF**, sufficiently distant from its boundaries.

### 3.2 Calibration pulser control

The **TPC** employs a calibration pulser system to inject charge onto the readout pads, allowing for testing of the full electronics processing chain with a well defined input signal. The pulser system employs one channel for each **GEM** stack, resulting in four channels per sector and 144 channels for the full **TPC**. The electronics is distributed into two crates with 72 channels each, one for each side of the detector. Similar to the laser control, the **UL** provides a 5 MHz pulser clock that is synchronized with the SAMPA sampling clock. When a pulser firing is requested—typically via the trigger system—the controller logic generates a signal aligned with the pulser clock and tailored to the interface requirements of the pulser system. Together with the pulser clock, this signal is transmitted to the pulser through the corresponding pulser **SyncBox**.

### 3.3 Readout of the high voltage current monitor system

The **HVCM** provides dynamic estimates of space charge generated by backflowing ions. They measure currents at the top electrode of the lowest **GEM** foil in every **GEM** stack (G4T) at a sampling rate of 1 kHz and with a resolution of 1 nA.<sup>26</sup> For the **TPC**, two **HVCM** crates are employed.

To ensure the recorded current data is immediately available and can be accurately correlated with regular detector data, readout and timestamp synchronization for these crates is implemented

---

<sup>25</sup>For Q-switch, flash, shutter, and camera synchronization, and a spare channel.

<sup>26</sup>The resolution is dominated by the capacitance of the 60 m long HV cables. The intrinsic resolution of the **HVCM** system has been measured to be 3 pA.

via the **UL** in the **CRU**. As shown in Fig. 23, each crate consists of nine front-end cards, each providing eight measurement channels. Each front-end card transmits a formatted data stream, including regular timestamps and current measurements, via universal asynchronous receiver/transmitter (UART) to a central controller card. The controller aggregates the incoming data, partitions it into chunks of 1 kB, and wraps each chunk with a header and trailer to form 1 KiB data frames. Each frame contains only payload originating from a single front-end card. These frames are output in a round-robin sequence and transmitted using 8b10b encoding over an **E-link** to a **VLDB**.

A similar crate, producing an identically formatted data stream, is installed to acquire current measurements from the central electrode and field cage. Although the data and resulting packet rates for the **HVCM** readout are relatively low, no packets may be lost, as all are required to reconstruct the full stream of **GEM** currents.

To allow precise temporal association of current data with detector events during offline analysis, a synchronized timestamp reset across all front-end streams is necessary. For this purpose, just before or at the start of a run, the **UL** forwards a selected trigger signal via the latency-deterministic **GBT** downlink to all connected **HVCM** crates. Within each crate, this reset signal is internally distributed to enforce simultaneous timestamp resets on all front-end cards.

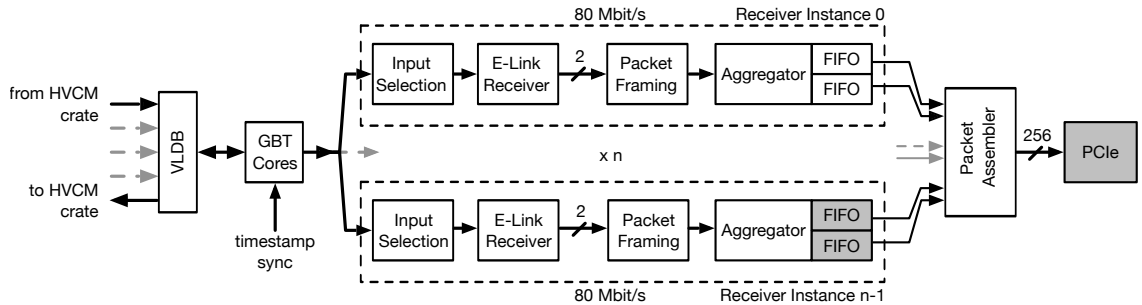


**Figure 24.** High-voltage current monitor readout chain.

The readout chain for the **HVCM** is shown in Fig. 24. The **VLDB** transmits monitoring data from all crates via the **GBT** to the **CRU**, at a rate of  $80 \text{ Mbit s}^{-1}$  per stream. On the **CRU**, dedicated receiver instances (one per stream) handle deserialization, decoding, and frame reassembly. The deserializer uses 8b10b idle symbols, which are guaranteed to appear at least between frames, to synchronize to the stream. As frames are reconstructed, their cyclic redundancy checks (CRCs) are performed to ensure flawless transmission. When a complete frame is received during a run, a corresponding frame descriptor is generated. Frames and descriptors are then buffered in FIFOs of appropriate depth.

The packet assembler polls the descriptor FIFO and begins packet creation whenever a descriptor is available. Each readout packet consists of an **RDH**, followed by a 256-bit **CRU** header. This header is constructed primarily from information in the descriptor and includes sequence numbers, timing metadata, and error flags. Finally, the packet is completed by appending the 1 KiB **HVCM** data frame.

## 4 Summary and discussion

Since the start of **LHC** operation in 2009, **FPGAs** have been a central component of data acquisition and online processing in the major experiments. Their reconfigurable logic, high I/O density, and deterministic timing make them ideally suited to handle the enormous bandwidths and low-latency requirements of modern detectors.

Over the last fifteen years, their role has shifted from basic data formatting to increasingly physics-aware online processing. ATLAS introduced FPGA-based calorimeter Feature Extractors to produce trigger primitives directly from finely segmented inputs [15]. LHCb adopted the TELL1 boards as its principal readout platform [16], where the **FPGAs** executed real-time preprocessing such as pedestal subtraction, zero suppression, and hit clustering. **ALICE** integrated large **FPGA** farms into its High Level Trigger (HLT) system, enabling online cluster finding, tracking, and calibration [17]. By Run 3, ATLAS [18], LHCb [9], and ALICE [10] had all transitioned to PCIe-based FPGA readout boards—including the widely adopted PCIe40 platform [8]—but with firmware stacks tailored to their specific detector architectures and processing requirements.

**ALICE**, in particular, has consistently pushed **FPGA**-based readout a step further. In Run 1, FPGA cluster finding enabled fast online processing in the **HLT** farm, while in Run 2, the **HLT** discarded raw data and stored only clusters and tracks [19]. In Run 3, the introduction of **CRUs** has extended the role of off-detector **FPGAs** into a full-fledged data conditioning and preprocessing layer between the detector front-ends and the **GPU**-based **EPNs**.

The approach adopted for the **ALICE TPC** in Run 3, described in this paper, emphasizes simplicity, robustness, and flexibility. On-detector logic was deliberately minimized: raw digitized signals are transmitted over deterministic-latency optical links based on the radiation-tolerant **GBT** chipset and Versatile Link components, shifting the processing burden to off-detector **FPGAs**, where algorithms can be more easily updated and refined as operational experience accumulates. Reliability was a guiding principle throughout; for example, the SAMPA chip can recover immediately after reset, restoring the full **TPC** front-end electronics in less than 400 ns. This approach has led to a very stable operation, where the readout of the **TPC** “just works”, no matter if radiation from collisions is present or not.

The **TPC UL** firmware described in this paper implements a suite of algorithms essential for the operation of the **TPC** and for an optimised performance. These include:

- common-mode correction across up to 1600 channels per **CRU**,
- ion-tail filtering and baseline correction,
- zero suppression, and
- dense data packing optimised for subsequent **GPU** processing.

In addition, it supports the online calibration tasks for the **TPC** by computing integrated digital currents, while carefully optimizing **FPGA** resources to maximize efficiency. The implemented functions provide the necessary data reduction and conditioning for high-throughput continuous readout. All functionality was extensively validated in simulation and with beam data, demonstrating reliable performance of the common-mode correction and other preprocessing steps.

Beyond data processing, the firmware also integrates the control of auxiliary subsystems, such as laser and pulser operation and the readout of high-voltage current monitors. Consolidating these functions into a single framework reduces heterogeneity and simplifies maintenance.

In summary, the [ALICE TPC](#) readout system combines lightweight on-detector electronics, radiation-tolerant optical links, and flexible off-detector [FPGA](#) processing into a robust solution. The processing meets the demands of unprecedented cluster and track densities at 50 kHz Pb–Pb collisions and applies the necessary corrections to achieve the required level of data quality. Through its careful balance of simplicity, reliability, and adaptability, the system provides the foundation for high-precision measurements in the challenging conditions of LHC Runs 3 and 4.

## Acknowledgements

We gratefully acknowledge the central [CRU](#) team for their support, expertise, and valuable discussions. We extend special thanks to Filippo Costa for his dedicated assistance, commitment, and prompt responses to all our questions and requests. His contributions have been invaluable to this work.

Furthermore, we acknowledge the following funding agencies for their support in the [TPC](#) Upgrade: Fundação de Amparo à Pesquisa do Estado de São Paulo (FAPESP), Brasil; Ministry of Science and Education, Croatia; The Danish Council for Independent Research | Natural Sciences, the Carlsberg Foundation and Danish National Research Foundation (DNRF), Denmark; Bundesministerium für Bildung, Wissenschaft, Forschung und Technologie (BMBF), GSI Helmholtzzentrum für Schwerionenforschung GmbH, DFG Cluster of Excellence "Origin and Structure of the Universe", The Helmholtz International Center for FAIR (HIC for FAIR) and the ExtreMe Matter Institute EMMI at the GSI Helmholtzzentrum für Schwerionenforschung, Germany; National Research, Development and Innovation Office, Hungary; Nagasaki Institute of Applied Science (IIST) and the University of Tokyo, Japan; Fondo de Cooperación Internacional en Ciencia y Tecnología (FONCICYT), Mexico; The Research Council of Norway, Norway; Ministry of Science and Higher Education and National Science Centre, Poland; Ministry of Education and Scientific Research, Institute of Atomic Physics and Ministry of Research and Innovation, and Institute of Atomic Physics, Romania; Ministry of Education, Science, Research and Sport of the Slovak Republic, Slovakia; Swedish Research Council (VR), Sweden; United States Department of Energy, Office of Nuclear Physics (DOE NP), United States of America.

## References

- [1] ALICE TPC collaboration, “The ALICE TPC, a large 3-dimensional tracking device with fast read-out for ultra-high multiplicity events”, *Nucl. Instr. Meth. A* **622** (2010) 316 [[1001.1950](#)].
- [2] ALICE TPC collaboration, “The upgrade of the ALICE TPC with GEMs and continuous readout”, *Journal of Instrumentation* **16** (2021) P03022.
- [3] ALICE collaboration, “Upgrade of the ALICE Experiment: Letter Of Intent”, *J. Phys. G* **41** (2014) 087001.

- [4] Z. Citron et al., “Report from Working Group 5: Future physics opportunities for high-density QCD at the LHC with heavy-ion and proton beams”, *CERN Yellow Rep. Monogr.* **7** (2019) 1159 [[1812.06772](#)].
- [5] ALICE TPC collaboration, “Correction of the baseline fluctuations in the GEM-based ALICE TPC”, *Journal of Instrumentation* **18** (2023) P11021.
- [6] Hernández, H. and others, “A monolithic 32-channel front-end and DSP ASIC for gaseous detectors”, *IEEE Transactions on Instrumentation and Measurement* **69** (2020) 2686.
- [7] L. Quaglia, “Recent results and upgrade of the ALICE muon spectrometer”, *Nuclear and Particle Physics Proceedings* **347** (2024) 75.
- [8] J. Cachemiche et al., “The PCIe-based readout system for the LHCb experiment”, *Journal of Instrumentation* **11** (2016) P02013.
- [9] LHCb collaboration, “The LHCb upgrade I”, *LHCb-DP-2022-002* (2023) [[2305.10515](#)].
- [10] ALICE collaboration, “Upgrade of the ALICE readout & trigger system”, *Technical Design Report, ERN-LHCC-2013-019* (2013) .
- [11] F. Costa, A. Kluge, P.V. Vyvre and for the ALICE Collaboration, “The detector read-out in ALICE during Run 3 and 4”, *Journal of Physics: Conference Series* **898** (2017) 032011.
- [12] O. Bourrion et al., “Versatile firmware for the common readout unit (CRU) of the ALICE experiment at the LHC”, *Journal of Instrumentation* **16** (2021) P05019.
- [13] R. Martin Lesma et al., “The Versatile Link Demo Board (VLDB)”, *JINST* **12** (2017) C02020.
- [14] G. Renault et al., “The laser of the ALICE Time Projection Chamber”, *International Journal of Modern Physics E* **16** (2007) 2413–2418.
- [15] B. Bauss et al., “Ultrascale+ for the new ATLAS calorimeter trigger board dedicated to jet identification”, *IEEE Nuclear Science Symposium and Medical Imaging Conference Proceedings (NSS/MIC)* (2018) .
- [16] G. Haefeli et al., “The LHCb DAQ interface board TELL1”, *Nucl. Instr. Meth. A* **560** (2006) 494.
- [17] ALICE, ATLAS collaboration, “The C-RORC PCIe card and its application in the ALICE and ATLAS experiments”, *JINST* **10** (2015) C02022.
- [18] ATLAS collaboration, “FELIX, the ATLAS readout system: From LHC Run 3 to Run 4”, *Technical Report, ATL-DAQ-PROC-2025-010* (2025) .
- [19] ALICE, “Real-time data processing in the ALICE High Level Trigger at the LHC”, *Computer Physics Communications* **242** (2019) 25.